Ocean Engineering 243 (2022) 110208

Contents lists available at ScienceDirect

Ocean Engineering

journal homepage: www.elsevier.com/locate/oceaneng

Development of a coupling algorithm for fluid-structure interaction analysis of submerged aquaculture nets

Hui Cheng [a,*], Muk Chen Ong [a], Lin Li [a], Hao Chen [b]

[a] Department of Mechanical and Structural Engineering and Materials Science, University of Stavanger, 4036, Stavanger, Norway
[b] School of Engineering, University of Glasgow, Glasgow, United Kingdom

ARTICLE INFO

Keywords:
Dynamic porous media model
Screen model
Fluid-structure interaction
Finite volume method
Finite element method
Aquaculture nets

ABSTRACT

A coupling algorithm between two open-source numerical toolboxes, *i.e.*, OpenFOAM and Code_Aster, is implemented for fluid-structure interaction analysis of submerged nets. This algorithm is developed to handle the wake effects of thin, flexible and highly permeable structures with complex geometries. Compared to previous approaches, the present algorithm simplifies the procedures of the model preparation by removing additional data-fitting processes for porous coefficients, and improves the accuracy of structural responses by employing a fluid solver to calculate the flow field and a superior Screen model to calculate the hydrodynamic forces. The coupling algorithm is comprehensively described and validated with published experiments for both fixed and flexible nets. Different solidities, inflow angles, incoming velocities and dimensions of nets are also considered. The comparisons of flow velocity in the wake, deformation of flexible nets and drag force on the full-scale fish cage show that the numerical results obtained from the present coupling algorithm are in good agreement with published experimental data.

1. Introduction

Global food fish consumption increases by 3.1% every year, averagely from 1961 to 2017, which is higher than that of all other animal protein foods (meat, dairy, milk, *etc.*) (Food and Agriculture Organization, 2020). The development of high-value finfish such as Atlantic Salmon (*Salmo Salar*) attracts significant investments in the aquaculture industry to upgrade conventional farming facilities and build novel aquaculture structures (Li et al., 2018), such as Ocean Farm 1 and Havfarm. These novel facilities require precise and reliable design to operate at offshore sites. Nets are one of the most critical components in aquaculture structures. According to the experiments reported by Cheng (2017), the environmental loads on nets account for more than 85% of the total loads on a gravity-based fish cage. In the engineering design process of aquaculture structures, the structural responses of nets under various current and wave conditions should be accurately predicted, so that support structures and mooring system can be properly designed.

In reality, an aquaculture structure usually comprises thousands of square metres of nets. These nets are usually flexible and can allow large displacements and deformations under currents and waves. The deformed nets can, in turn, affect the flow field. The affected flow field can significantly affect the structural responses of the nets and the global movement of aquaculture structures (Bi et al., 2013; Cheng et al., 2020; Zhao *et al.*, 2013a,b). Two major challenges arise in predicting structural responses of such large and flexible structures under complex environmental conditions: (1) model the large-scale flexible nets with a feasible method and (2) correctly assign environmental loads on flexible nets.

The first challenge arises as it is impractical to directly model the whole nets in aquaculture structures by each twine. The nets in an aquaculture structure usually comprise millions of twines which require an enormously large number of elements for modelling. For example, more than 30 million one-dimensional elements are needed to directly model the nets in the aquaculture structure, as shown in Fig. 1(b). Besides the one-dimensional elements, mass-spring element and triangular element are often employed to calculate the structural responses of nets. Lee et al. (2008), Takagi et al. (2004) and Zhao et al. (2007) used a mass-spring model to calculate the structural responses of both trawling nets and fish cages. Tsukrov et al. (2003) proposed a consistent finite element (a class of one-dimensional element) to analyse structural responses of offshore aquaculture fish cages under waves and currents. Priour (2013) proposed a triangular element for net panels and successfully predicted the deformation of fishing net and fish cage (Priour, 2014; Moe-Føre et al., 2015). No matter which structural model is

* Corresponding author.
E-mail address: hui.cheng@uis.no (H. Cheng).

https://doi.org/10.1016/j.oceaneng.2021.110208
Received 22 June 2021; Received in revised form 18 October 2021; Accepted 13 November 2021
Available online 1 December 2021

Nomenclature

A_t	outline area of a net panel
C_D	drag force coefficient of a net panel
C_L	lift force coefficient of a net panel
d_{w0}	physical twine diameter
d_{ws}	structural diameter
d_{we}	elastic diameter
d_{wh}	hydrodynamic diameter
E	Young's modulus
e_n	unit normal vector of a net panel
L	half mesh size of net
α	porosity of porous zone
r_u	flow reduction factor
Sn	solidity of a net panel
T	thickness of the porous zone
$\boldsymbol{U}_{-\infty}$	undisturbed incoming flow velocity
$\boldsymbol{U}_{+\infty}$	flow velocity in the wake
$\boldsymbol{U_c}$	flow velocity at the centroid of a net panel
$\boldsymbol{u}$	velocity of fluid
$\boldsymbol{v}$	velocity of structure
ρ_w	density of fluid
ρ_s	density of solid
λ	mesh grouping factor
θ	inflow angle, where $\theta = 0°$ indicates that the flow is aligned with the normal direction of a net panel

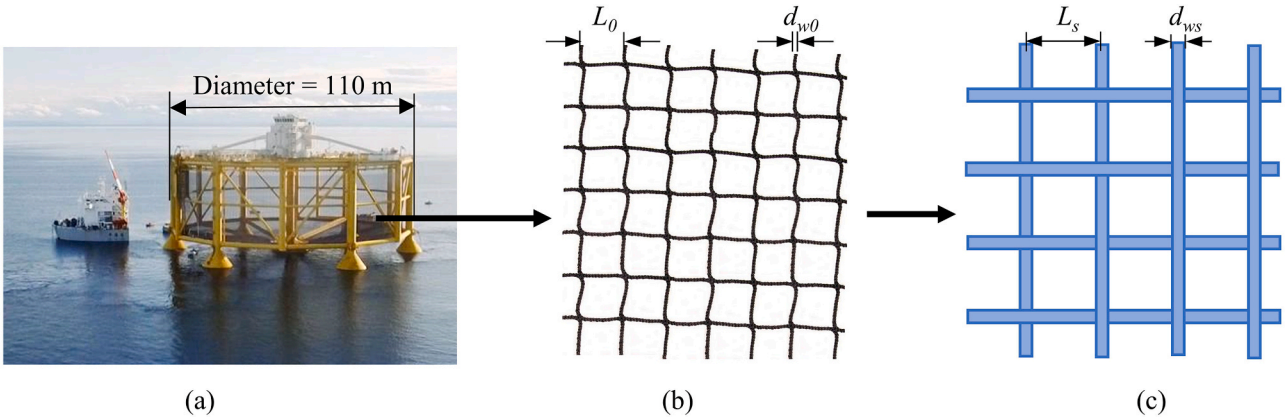

Fig. 1. Illustration of nets in an offshore aquaculture structure and the "mesh grouping" method. (a) A large aquaculture structure with a diameter of 110 m and a height of 67 m (SalMar ASA). (b) A piece of typical nets in aquaculture structures with a mesh size L_0 of 30–50 mm and a twine diameter d_{w0} of 2–4 mm. (c) The nets are represented by one-dimensional finite elements in the present structural model using a "mesh grouping" method.

employed, a "mesh grouping" method, in which several actual meshes are grouped into fictitious meshes that have equivalent masses, weights and environmental loads, is usually adopted in the modelling progress in order to reduce the computational effort (Tsukrov et al., 2003; Huang et al., 2019). Within a proper "mesh grouping" method, Moe-Føre et al. (2015) demonstrated that mass-spring elements, bar-like elements, and triangular elements have similar results in terms of nets deformation. Zhao et al. (2015) showed that mass-spring elements and truss elements could reproduce the experimental results with similar accuracy, but the model using mass-spring elements had approximately twice the number of nodes as the model using truss elements. Given the above research works, the three types of elements can predict the structural responses of nets, based on a proper "mesh grouping" method.

The second challenge is crucial for modelling nets under the actions of current and waves. The environmental loads on the nets are usually predicted using a hydrodynamic force model, which is the key to determine external forces for structural analyses. In order to acquire an accurate hydrodynamic force model, researchers have conducted considerable flume experiments and theoretical analyses. In general, two types of hydrodynamic force models are commonly used to calculate the environmental loads on nets, *i.e.*, Morison model (DeCew et al., 2010; Zhao et al., 2007) and Screen model (Aarsnes et al., 1990; Lee et al., 2008; Balash et al., 2009; Kristiansen and Faltinsen, 2012). The main difference between the two types of models is the object of reference for calculating the environmental loads. The Morison model takes a single twine as the object, while the Screen model takes a flat net panel as the object. A systematic comparison between the two types of hydrodynamic force models was shown in Cheng et al. (2020), where the authors suggested employing the Screen model for a cylindrical fish cage to amend the defects of Morison models.

In a real fish farm, nets at different positions usually experience different flow velocities due to wake effects. In the context of aquaculture structures, the wake is the region downstream from the permeable nets, where the velocity is reduced and the flow is often turbulent (Cheng et al., 2020; Sim et al., 2021; Zhao et al., 2013a, 2013b). For a typical cylindrical fish cage, approximately half of the nets, located at the rear side of the cage, experience the wake flow generated by the front part of the cage. Thus, knowing how the flow velocity is reduced in the wake is the key for calculating the forces on aquaculture structures, particularly since the force is proportional to the square of velocity in the hydrodynamic force models, giving a large contribution (Lekang, 2019). Neglecting the wake effects in numerical analyses can cause unreliable structural responses of the whole fish cage (Chu et al., 2020; Rickard, 2020; Chen et al., 2021). According to the study by Faltinsen and Shen (2018), the anchor force of a single fish cage can increase by up to 22% if wake effects are not included in numerical analyses. Moreover, the wake effects play a vital role in the design of a fish farm which is usually comprised of several fish cages (Bi and Xu, 2018; Sim et al., 2021).

Different methods have been proposed to estimate the wake effects for aquaculture structures. In general, they can be categorised into two approaches. The first approach is to assign a pre-defined empirical flow reduction factor (r_u) onto the downstream nets in order to lower the hydrodynamic forces. The value of r_u can be acquired from theoretical analyses and experimental results. Løland (1991) proposed an engineering approach, *i.e.*, $r_u = 1–0.46C_{D(\theta\,=\,0°)}$ where C_D is the drag coefficient of a net panel and θ is the inflow angle, to calculate the flow

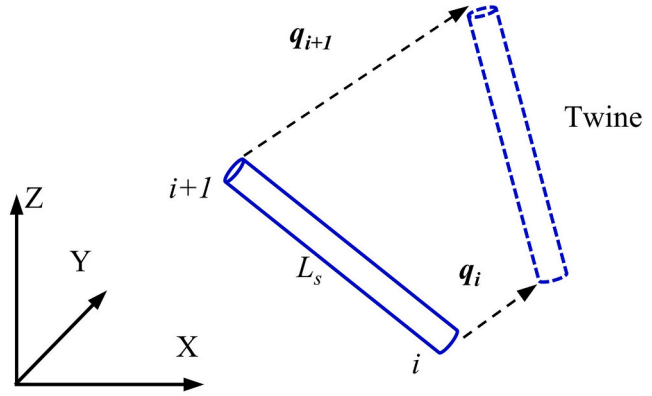

Fig. 2. Illustration of the "CABLE" element.

reduction factor. Lee et al. (2008) conducted water-tank experiments with plane nets under different inflow angles, solidity and flow velocities, and found that r_u reduced with increasing inflow angles. Cheng et al. (2020) proposed a new formula based on previous experimental data, considering both the solidity and inflow angle of net panels. The new formula showed a better agreement with experimental results than the previous methods. However, the first approach simplifies the wake effect by assigning a constant r_u onto the downstream nets to turn down the hydrodynamic forces, without considering the directions of the flow. The second approach is to solve the fluid field through and around aquaculture structures using proper fluid models. Recently, the computational fluid dynamic (CFD) method combined with a porous media model was proposed by Simonsen et al. (2006) to calculate the flow field around nets. The advantage of this method is that it is not necessary to conduct numerous experiments to acquire r_u, which can save considerable time and cost. Patursson et al. (2010) applied experiment-based porous media resistance coefficients in ANSYS Fluent to model the flow through and around nets. Their promising results inspire researchers to combine the CFD method with commonly used finite element methods. Further studies showed that combining CFD simulations and structural analyses can acquire more accurate structural responses than pure structural analyses (Bi et al., 2014a; Yao et al., 2016). Moreover, results from CFD simulations are valuable for the understanding of nutrients and materials transport (Alver et al., 2016; Oppedal et al., 2011) and pollutant distribution (Xu and Qin, 2020) in fish farming sites. Thus, combining CFD simulations and structural analyses has become a new trend in the design of aquaculture structures.

The interaction between flexible nets and fluid is a typical fluid-structure interaction (FSI) problem and requires solving the governing equations in both the fluid and structure domains. For this FSI problem, one of the most noticeable contributions is the immersed boundary method (IBM), which was initially proposed by Peskin (1972). The interaction between the fluid and structure is usually accomplished by distributing nodal forces and interpolating nodal velocities between the Eulerian and Lagrangian domains using the Dirac delta function (Wang and Zhang, 2009). Because flexible nets can experience large deformations in the three-dimensional domain, a class of non-boundary-fitted method is usually chosen to track the moving boundaries (Wang et al., 2017). In this method, the fluid domain and solid domain are discretised separately using fixed Eulerian grids and moving Lagrangian grid, respectively. Due to the separated discretisation, the coupling information cannot be transferred between the two domains directly. Thus, it is challenging to build the relation for these two independents meshes to impose the coupling condition (de Tullio and Pascazio, 2016; Jiang et al., 2018). Moreover, according to Yan et al. (2020), the conventional IBM had a major disadvantage for fibre-like immersed structures, *e.g.*, the cables and nets in the present study, because fibre-liked structures occupy negligible volume in the fluid domain. Thus, a new coupling algorithm is needed to study the effect of nets, which are thin (2–4 mm of twine diameter), flexible and highly permeable structures, on the flow field through and around a large aquaculture structure (hundreds of metres) in a computationally affordable way.

In the present study, the fluid and structure are discretised separately and described using fixed Eulerian grids and one-dimensional bar-like elements, respectively. The hydrodynamic forces on nets are calculated based on the advanced Screen model. Details about the numerical models and coupling algorithm are introduced in Section 2. In Section 3, a series of experiments conducted by Patursson et al. (2010), Bi et al. (2014a), and a full-scale test by Gansel et al. (2018) are reproduced to validate the present method. Finally, the results of this study are summarised with concluding remarks.

2. Numerical models and coupling algorithm

In the present study, the structural model is solved by Code_Aster, while the fluid model is solved by OpenFOAM. The two solvers are well-verified according to the research works by Févotte and Lathuilière (2017) for Code_Aster and Robertson et al. (2015) for OpenFOAM.

2.1. Structural model

2.1.1. Governing equations

The structural responses are calculated based on the Finite Element Method (FEM), where the net is divided into a set of one-dimensional elements. The equation governing the motions of Lagrangian nodes in the Cartesian coordinate system is:

$$[\boldsymbol{M}]\ddot{\boldsymbol{q}} + [\boldsymbol{K}]\boldsymbol{q} = \boldsymbol{F_g} + \boldsymbol{F_b} + \boldsymbol{F_h} \tag{1}$$

where $\boldsymbol{q}$ is the time-dependent vector of nodal displacements, $\boldsymbol{M}$ is the mass matrix, $\boldsymbol{K}$ is the stiffness matrix, $\boldsymbol{F_g}$ is the nodal force vector due to gravity, $\boldsymbol{F_b}$ is the nodal force vector for buoyancy forces, and $\boldsymbol{F_h}$ is the nodal force vector for the hydrodynamic forces, which is discussed in Section 2.2. $\boldsymbol{F_g}$ and $\boldsymbol{F_b}$ are simple and only calculated one time in the initialisation step, and they are constant throughout numerical simulations.

The system is highly nonlinear because $\boldsymbol{F_h}$ depends on the time, the square of nodal velocities, and the structural deformations, see Eqs. (6) and (7). According to Antonutti et al. (2018), the system nonlinearity can cause high-frequency oscillations and bring challenges for the simulations to reach convergence. In the present structural solver, the solution technique for Eq. (1) is based on the unconditionally stable Hilber-Hughes-Taylor- α (HHT-α) method, which introduces low numerical damping in the low-frequency band and high damping at the high-frequency band. In the simulations presented in Section 3, the value of the numerical damping is chosen by gradually increasing the damping until the reaction forces become free of high-frequency noise.

2.1.2. Finite element constitution

The structural element used in the present study is a one-dimensional finite element denoted as “CABLE” in the structural solver, which was initially developed to calculate the mechanical behaviour of overhead electrical lines. This element is a version of the classic two-node “bar” element but can only bear tensions. It is suitable for representing highly flexible line-like structures (Antonutti et al., 2018), and thus, suitable for modelling cable and nets. As illustrated in Fig. 2, one “CABLE” element has six nodal degrees of freedom (DOFs, three components at each node) in the global coordinate system, which correspond to the translations at its two nodes. Linear shape functions ($\boldsymbol{N}$) are used to express the deformation of the element ($\widehat{q}$) in the global coordinate system as a function of the vector of DOF ($\boldsymbol{q}$):

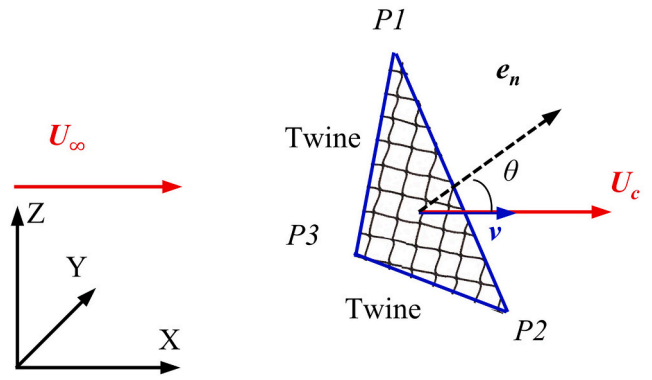

Fig. 3. Illustration of a virtual panel. The inflow angle θ of the virtual panel element is defined as the angle between $\boldsymbol{e_n}$ and $\boldsymbol{U_c}$.

$$\hat{\boldsymbol{q}} = \begin{bmatrix} 1-\xi & 0 & 0 \\ 0 & 1-\xi & 0 \\ 0 & 0 & 1-\xi \end{bmatrix} \begin{bmatrix} q_x^i \\ q_y^i \\ q_z^i \end{bmatrix} + \begin{bmatrix} \xi & 0 & 0 \\ 0 & \xi & 0 \\ 0 & 0 & \xi \end{bmatrix} \begin{bmatrix} q_x^{i+1} \\ q_y^{i+1} \\ q_z^{i+1} \end{bmatrix} \tag{2}$$

where ξ is the strain, and the two square matrixes are the shape functions ($\boldsymbol{N}$).

$$[\boldsymbol{M}] = \frac{\rho_s \pi d_{ws}^2}{4} \int_{x=0}^{L_s} NN^T dx \tag{3}$$

$$[\boldsymbol{K}] = \frac{\pi d_{we}^2 E}{4} \int_{x=0}^{L_s} BB^T dx \tag{4}$$

The mass matrix ($\boldsymbol{M}$) and stiffness matrix ($\boldsymbol{K}$) for one structural element are shown in Eqs. (3) and (4), where $\boldsymbol{B} = \boldsymbol{J}-1\frac{\partial N}{\partial x}$ is the element strain-displacement transformation matrix, $\boldsymbol{J}$ is the Jacobian matrix, d_{ws} is the structural diameter, d_{we} is the elastic diameter, and L_s is the length of one element. After assembling contributions from individual elements and concentrating all the environmental loads to nodes, the structural responses are calculated using Eq. (1). Because the dimensions of aquaculture structure and net mesh size are significantly different, direct modelling the whole nets is impractical. In order to achieve equivalent numerical results, a "mesh grouping" method is employed in the present study. The detailed derivation and explanation can be referred to Cheng et al. (2020). Here, only the relationships between the derived diameters and the physical twine diameter (d_{w0}) for nets with square meshes are presented:

$$\lambda = L_s \Big/ L_0;\ d_{ws} \approx \sqrt{\lambda} d_{w0};\ d_{wh} = \lambda d_{w0} \tag{5}$$

where λ is the mesh grouping factor which is defined as the ratio between the half mesh size of the numerical net L_s and the actual net L_0. For a full-scale fish farm facility, λ is usually in the range of 20–80.

2.2. Hydrodynamic force model

As the hydrodynamic forces on nets are complex, a hydrodynamic force model is required to calculate the forces on structures and transfer the forces to the structural solver. In the present study, hydrodynamic forces on nets are calculated based on Screen models. Screen models are theoretically superior to Morison models as the twine-to-twine interaction is implicitly considered in the force calculation (Cheng et al., 2020). The hydrodynamic forces ($\boldsymbol{F_h}$) are usually decomposed into drag force $\boldsymbol{F_D}$ and lift force $\boldsymbol{F_L}$ (*i.e.*, $\boldsymbol{F_h} = \boldsymbol{F_D} + \boldsymbol{F_L}$). Fig. 3 illustrates a virtual panel element for calculating hydrodynamic forces in the present study. The equations for $\boldsymbol{F_D}$ and $\boldsymbol{F_L}$ are shown as follows:

$$\boldsymbol{F_D} = \frac{1}{2} C_D \rho_w A_t \left| \boldsymbol{U}_{-\infty} - \boldsymbol{v} \right|^2 \boldsymbol{i_D} \tag{6}$$

$$\boldsymbol{F_L} = \frac{1}{2} C_L \rho_w A_t \left| \boldsymbol{U}_{-\infty} - \boldsymbol{v} \right|^2 \boldsymbol{i_L} \tag{7}$$

$$\boldsymbol{i_D} = \frac{\boldsymbol{U}_{-\infty} - \boldsymbol{v}}{|\boldsymbol{U}_{-\infty} - \boldsymbol{v}|} \tag{8}$$

$$\boldsymbol{i_L} = \frac{(\boldsymbol{U}_{-\infty} - \boldsymbol{v}) \times e_n \times (\boldsymbol{U}_{-\infty} - \boldsymbol{v})}{|(\boldsymbol{U}_{-\infty} - \boldsymbol{v}) \times e_n \times (\boldsymbol{U}_{-\infty} - \boldsymbol{v})|} \tag{9}$$

where ρ_w is the fluid density, A_t is the area of a virtual net panel (*i.e.*, the area of the triangular P1–P2–P3 in Fig. 3), $\boldsymbol{U}_{-\infty}$ is the undisturbed incoming flow velocity in the upstream of the net panel, $\boldsymbol{v}$ is the velocity of the structure. The unit vectors $\boldsymbol{i_D}$ and $\boldsymbol{i_L}$ which are used to indicate the directions of forces are defined by Eqs. (8) and (9). C_D and C_L are the drag and lift force coefficients in Screen models, respectively. These force coefficients are usually obtained from experiments that approximate the ideal conditions of a finite net panel in an infinite flow field. However, these ideal conditions are challenging to achieve in practice. An example is given in Section 3.3, showing the effect of the

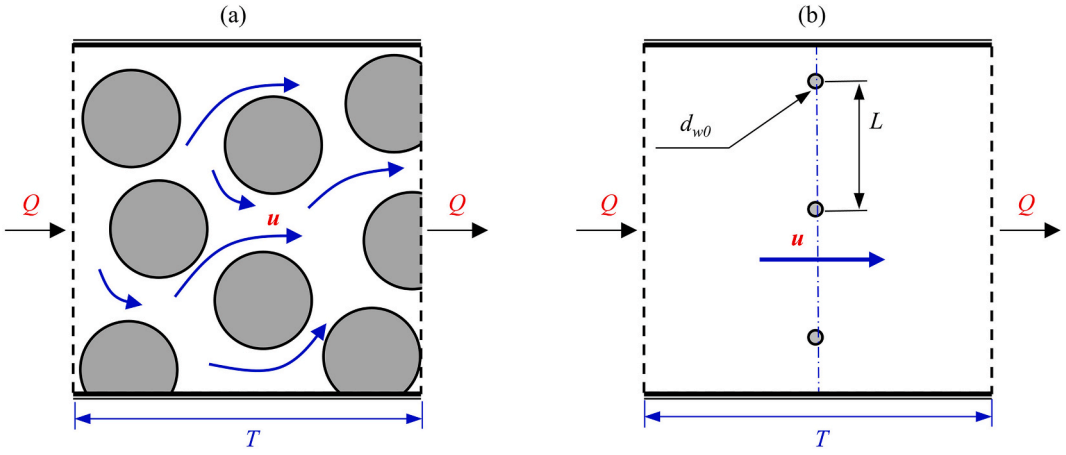

Fig. 4. A 2D illustration of the velocity at the cell centroid ($\boldsymbol{U_c}$) with different porous media models. The dark grey circles represent solid. A square box represents one cell in the fluid solver. Based on the conservation of mass, the flux Q through the cell is constant, which leads to an increasing velocity $\boldsymbol{u}$ in the pore area. (a) In the commonly used porous media model for coastal structures, the solids are filled in the porous zone and increased the intrinsic velocity (Jensen et al., 2014). (b) In the dynamic porous media (DPM) model for nets, the fibre-like solids (twines) concentrate along a line and occupy a negligible volume of the porous zone.

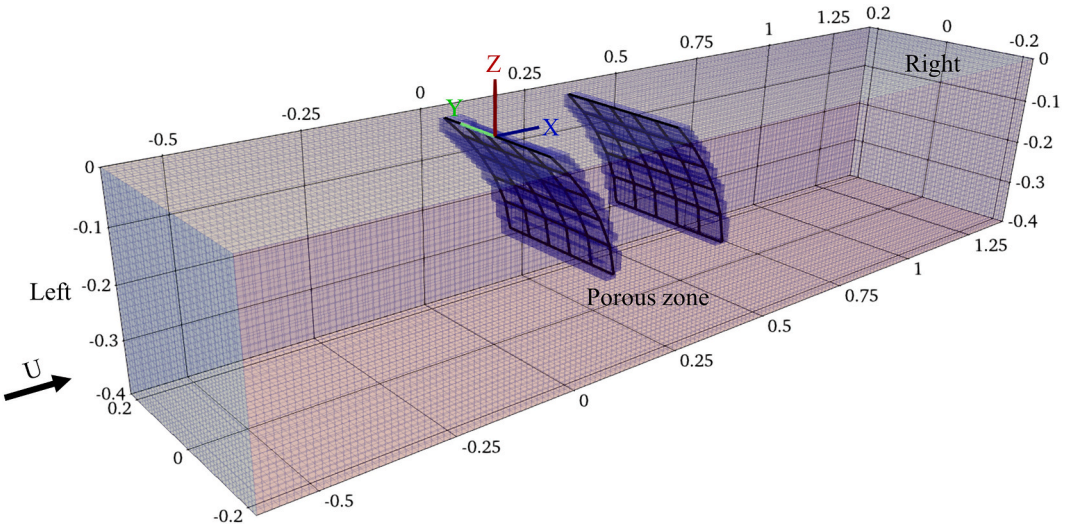

Fig. 5. Illustration of the computational domain for fluid. This illustration corresponds to the validation case in Section 3.3. The blue cells represent the porous zones in the fluid model. The black lines inside the porous zones are the structural model, which is composed of one-dimensional elements. (For interpretation of the references to colour in this figure legend, the reader is referred to the Web version of this article.)

experimental conditions on C_D and C_L.

Usually, the force coefficients (*i.e.*, C_D and C_L) in the existing hydrodynamic force models are derived based on the undisturbed flow velocity $\boldsymbol{U}_{-\infty}$, because the value of $\boldsymbol{U}_{-\infty}$ is easy to measure in laboratory experiments (*e.g.*, the towing speed in towing tank experiments or the flow velocity in recirculating flume experiments). One should notice that $\boldsymbol{U}_{-\infty}$ can be different for nets at the different positions of an aquaculture structure due to the wake effects. The different $\boldsymbol{U}_{-\infty}$ brings challenges to calculate the hydrodynamic forces on the nets. In the present study, the wake effects are solved by a fluid model, and the flow velocity at the centroid of a virtual panel element $\boldsymbol{U_c}$ can be obtained directly from the fluid solver. In order to employ the existing hydrodynamic force model in Eqs. (6) and (7), $\boldsymbol{U}_{-\infty}$ must be expressed in terms of $\boldsymbol{U_c}$. The final relationship between $\boldsymbol{U}_{-\infty}$ and $\boldsymbol{U_c}$ is presented in Eq. (10), and the detailed derivations can be found in the Appendix.

$$\boldsymbol{U}_{-\infty} = \sqrt{\frac{2}{2-(C_D+C_L)}}\boldsymbol{U_c} \tag{10}$$

2.3. Fluid model

2.3.1. Governing equations

In the present study, the flow field is calculated based on the Finite Volume Method (FVM), and the fluid domain is divided into a grid of cells. The equations governing the incompressible flow based on Eulerian cells include a continuity equation and momentum equations:

$$\nabla\cdot\boldsymbol{u} = 0 \tag{11}$$

$$\frac{\partial \boldsymbol{u}}{\partial t} + \boldsymbol{u}\cdot\nabla\boldsymbol{u} = -\frac{1}{\rho}\nabla p + \nabla\cdot\left[(\nu+\nu_T)\left(\nabla\boldsymbol{u}+\nabla\boldsymbol{u}^T\right)\right] + \boldsymbol{g} + \boldsymbol{S}_{pz} \tag{12}$$

where $\boldsymbol{u}$ is the velocity of the fluid, p is the pressure, ν is the fluid kinematic viscosity, ρ is the fluid density, $\boldsymbol{g}$ is the gravity acceleration, $\boldsymbol{S_{pz}}$ is the source term due to the existence of net. The source term $\boldsymbol{S_{pz}}$ is added to the cells in porous zones to account for the resistance force from nets. A dynamic porous media (DPM) model is developed to find the porous zones (shown as blue cells in Fig. 5) and to assign the correct $\boldsymbol{S}_{pz}$ onto the exact cells. Explanations for the DPM model are presented in Section 2.4.

Unlike the porous media models for coastal structures (Jensen et al., 2014), the present DPM model does not need to modify $\boldsymbol{u}$ in governing equations. As shown in Fig. 4, $\boldsymbol{U_c}$ is the fluid velocity at the cell centroid, which is defined as a volume-averaged velocity where averaging is done over the volume containing both fluid and solid domains. For Fig. 4 (a), $\boldsymbol{U_c}$ is no doubt smaller than the intrinsic averaged velocity ($\boldsymbol{U_{ia}}$) where the averaging is done over the fluid domain only. According to the conservation of mass, the relationship between $\boldsymbol{U_c}$ and $\boldsymbol{U_{ia}}$ can be expressed as $\boldsymbol{U_c} = \alpha\boldsymbol{U_{ia}}$, where α is the porosity of the porous zone, defined as the ratio of the volume occupied by the fluid to the total volume of the porous zone. For Fig. 4 (b), α can be calculated as:

$$\alpha = \frac{A_t T - \frac{\pi}{4} Sn A_t d_{w0}}{A_t T} = 1 - \frac{\pi}{4}\frac{d_{w0}}{T}Sn \tag{13}$$

where Sn is the solidity of nets, d_{w0} is the diameter of the actual twine, A_t is the area of a net panel, and T is the thickness of the porous zone. As illustrated in Fig. 1, the twine diameter is in the order of 10^{-3} m, and the dimension of a whole fish cage is in the order of 10^2 m. With different such a broad range of scales in dimension, it would be computationally unaffordable to model the fluid with a fine mesh that can capture the complex flow separation from the twines. Furthermore, such a complex and high-resolution flow field around small twines might be redundant for the design of aquaculture structures. Thus, for the fibre-like structure in the present study, the thickness of the porous zone is much larger than the diameter of the actual twine. Hereby, $T \gg d_{w0}$ and $\alpha \approx 1$ based on Eq. (13). Thus, the porosity is unnecessary to include in the governing equations.

As observed in the experiments by Bi et al. (2013), a transition zone is formed near a net panel due to different flow velocities inside and outside the wake. The flow in the transition zone is a typical free shear flow. Chen and Christensen (2017) compared four types of turbulence models, *i.e.*, k-ε model, k-ω model, k-ω SST model and realisable k-ε model, to simulate this free shear flow near a net. According to the reported comparisons, these four turbulence models give similar results regarding the flow velocities in the wake. Thus, the k-ε model of Jones and Launder (1972) is used in the present study as the turbulence closure for the RANS equations.

$$\frac{Dk}{Dt} = \nabla\cdot[(\nu+\sigma_k\nu_T)\nabla k] + G_k - \varepsilon \tag{14}$$

$$\frac{D\varepsilon}{Dt} = \nabla\cdot[(\nu+\sigma_\varepsilon\nu_T)\nabla\varepsilon] + C_{1\varepsilon}\frac{\varepsilon}{k}G_k - C_{2\varepsilon}\frac{\varepsilon^2}{k} \tag{15}$$

$$G_k = \frac{\nu_T}{2}\left(\nabla\boldsymbol{u}+\nabla\boldsymbol{u}^T\right)^2 \tag{16}$$

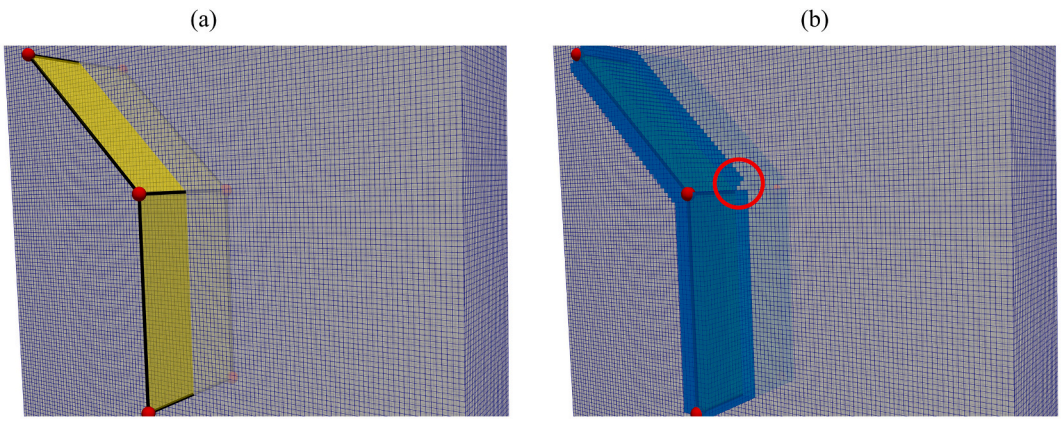

Fig. 6. Illustration of the topological method. (a) The yellow rectangles represent the virtual net panels with different θ. The red points represent the vertexes that define the location of the virtual net panels. The black lines represent the "CABLE" elements. (b) The blue cells are the porous zones in the fluid domain. The red circle indicates the missing cells. (For interpretation of the references to colour in this figure legend, the reader is referred to the Web version of this article.)

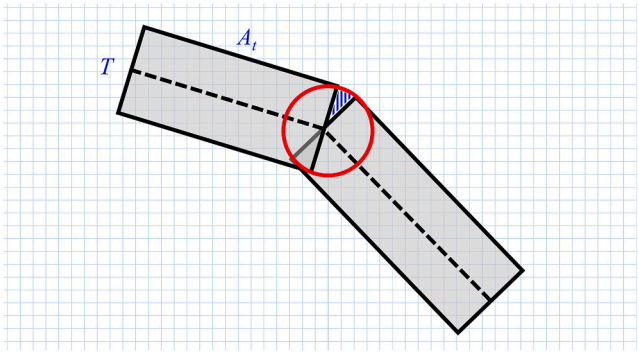

Fig. 7. Two-dimensional illustration of the improved topological method in the present study. When it comes to three-dimensional space, the two black rectangles represent the porous zones that are extruded by a thickness of T based on the virtual net panels, and the red circle represents a circular cylinder that is extruded along the common edges of two adjacent net panels. (For interpretation of the references to colour in this figure legend, the reader is referred to the Web version of this article.)

$$\nu_T = C_\mu \frac{k^2}{\varepsilon} \tag{17}$$

where $\sigma_k = 1.0$, $\sigma_\varepsilon = 1.3$, $C_{1\varepsilon} = 1.44$, $C_{2\varepsilon} = 1.92$, $C_\mu = 0.09$. The initial values of the turbulence quantities (k and ε) are estimated as follows:

$$k = \frac{3}{2}(\boldsymbol{u}I)^2;\ \varepsilon = \frac{C_\mu^{0.75} k^{1.5}}{L_T} \tag{18}$$

where I is the turbulence intensity, L_T is the turbulence length scale.

The effect of nets is negligible in turbulence modelling. Physically, when the flow passes through a net, the turbulent kinetic energy (TKE) can increase around the net due to the existence of individual twines in the net, but TKE dissipates very fast with a power law in the wake region (Laws and Livesey, 1978). In order to precisely model the turbulence around a net, extensive studies and well-validated experimental data are needed. However, for a typical fish cage in which the distance between upstream net and downstream nets is usually from 20 to 50 m (Halwart et al., 2007), the TKE generated by the upstream nets should dissipate into negligible scale before the flow travels to the downstream nets. Thus, the additional terms to address TKE are not included in Eqs. (12) and (13).

2.3.2. Boundary conditions for fluid

The flow field is solved using the Pressure Implicit with Splitting of Operators (PISO) algorithm. The spatial schemes for gradient, Laplacian and divergence are Gauss linear, bounded Gauss linear upwind, and Gauss linear limited corrected. All the simulations in Section 3 are three-dimensional and with a similar fluid domain, as shown in Fig. 5. The boundary conditions for fluid are listed as follows:

(1) Left: A uniform velocity is given as the inlet condition. p is set as zero normal gradient. The values of $\boldsymbol{u}$, k and ε on the left boundary vary in different cases and will be given along with the description of each case in Section 3.
(2) Right: A fixed zero pressure is set as outlet condition. $\boldsymbol{u}$, k, and ε are set as zero normal gradient.
(3) Top, bottom, front and back: p, k, and ε are specified as zero normal gradient. $\boldsymbol{u}$ is set as a slip condition. According to Patursson (2008), near-wall treatment has a negligible effect on the numerical results when the nets are far away from the wall. Thus, no near-wall treatment is employed in the simulations.

2.4. Dynamic porous media model

The porous zones, representing nets in the fluid domain, are governed by a dynamic porous media (DPM) model in the present study. Two main functions in this model, i.e. (1) find the cells that belong to the porous zones, and (2) assign the correct $\boldsymbol{S}_{pz}$ onto the exact cells, are explained in detail in Section 2.4.1 and 2.4.2, respectively.

2.4.1. Topological method

In order to represent the deformation of nets in fluid, a topological method is needed to map the Lagrangian nodes to the Eulerian grids. As the nets are flexible and can have violent movements under strong current flows, it is challenging for the fluid solver to identify the positions of the net panels. In the present study, an improved topological method is developed based on the research work reported by Chen and Christensen (2017) to map the geometries. As discussed by Martin et al. (2020) and Chen and Christensen (2017), the original method can lead to missing cells (the circled cells in Fig. 6(b)) at intersections of porous zones when the two adjacent net panels have different θ. These missing cells can have side effects on the downstream wake when the net has large deformation.

In order to address the problem of missing cells, an improved topological method is developed in the present study. A cell is recognised in porous zones if its centroid is located in the volume extruded based on virtual panel elements by a thickness of T. Besides, an additional procedure is introduced to retrieve the missing cells. As illustrated in Fig. 7, the red circle (with a diameter of D) between the two porous zones (with a thickness of T) covers the gaps and retrieve the missing cells in the

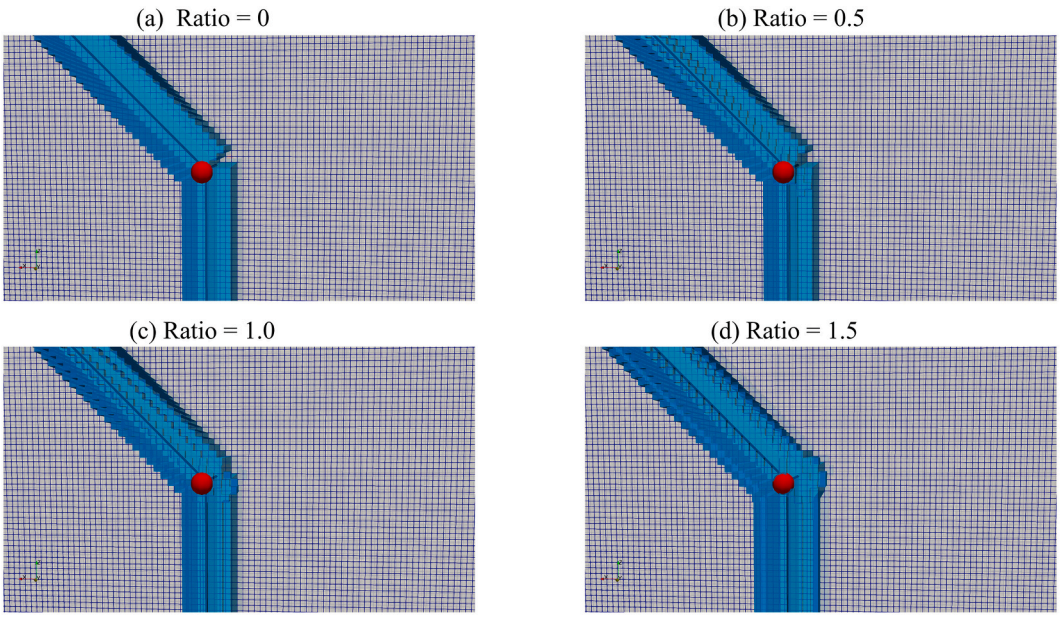

Fig. 8. The effect of different D/T on cell retrieval.

gaps. The ratio of D/T determines how many cells in the gaps can be retrieved. Fig. 8 shows the influence of D/T on the cell retrieval. $D/T = 0$ corresponds to the results of the original topological method proposed by Chen and Christensen (2017). With increasing D/T, more fluid cells at intersections of porous zones are retrieved. The present study adopts $D/T = 1$, as it can retrieve exactly all the missed cells in the gaps, neither more nor less than expected. Apart from the red circle, a conditional statement is added to exclude duplicated cells. Thus, the volume of one porous zone, V_{pz}, can be expressed as follows:

$$V_{pz} = TA_t = \sum_{i=1}^{m} V_i \tag{19}$$

where m is the number of cells in one porous zone, A_t is the area of one virtual net panel, and V_i is the volume of a fluid cell.

2.4.2. Conservation of momentum

As shown in Fig. 1(b), nets consist of millions of small twines in an aquaculture structure. The twines are intersected with each other and forming a porous membrane-like structure. In various industrial situations where a well-resolved grid or even a reduced resolution grid is unaffordable, a porous media model is usually adopted to study the flow field around the porous structure (Roelofs and Shams, 2019). Essentially, a porous media model handles the flow field by adding an extra momentum source term in the governing momentum equations (the $\boldsymbol{S_{pz}}$ in Eq. (11)). According to the study by O'Neill (2006), the source term can be expressed by a polynomial function of the velocity at the cell centroid, and expressed using the following general form:

$$\boldsymbol{S_{pz}} = \sum_{i=1}^{n} C_i \boldsymbol{u_c}^i \tag{20}$$

where the coefficients C_i are acquired by data fitting, n is the degree of the polynomial, and $\boldsymbol{u_c}$ is the velocity of the fluid. Usually, $n = 2$ is sufficient for most engineering applications (O'Neill, 2006). In the present study, the value of $\boldsymbol{S_{pz}}$ is calculated based on the conservation of momentum instead of the data fitting from fluid experiments that measure the pressure difference (*e.g.*, experiments by Zhong et al. (2014)).

The conservation of momentum should be fulfilled during the data exchange between the fluid and structural solvers. Based on Newton's Third Law, the hydrodynamic forces on nets and the resistance forces on the fluid are equal in magnitude and opposite in direction. Thus, the relation between the hydrodynamic force on a single virtual panel element and the loss of the fluid momentum in the corresponding porous zone can be expressed by Eq. (21), where the volume integral is conducted over the porous zone.

The purpose of adopting a porous media model in the present study is not to study the complex flow separations near the nets, but to handle the wake effects in the region downstream of the nets. Thus, $\boldsymbol{S_{pz}}$ can be treated as a constant through the cells in a porous zone which represents a single virtual panel in the fluid domain. Hereby, the volume integral on the left-hand side of Eq. (21) reduces to the product of the volume of a porous zone (TA_t) and $\boldsymbol{S_{pz}}$, as given in Eq.(22). On the right-hand of Eq. (22), the hydrodynamic force $\boldsymbol{F_h} = \boldsymbol{F_D} + \boldsymbol{F_L}$, and is calculated using Eqs. (6) - (9). Together with Eq. (10), the value of source term in one fluid cell with a volume of V_i can be written as Eq.(23) for convenience.

$$\iiint_V \rho_w \boldsymbol{S_{pz}} \boldsymbol{dxdydz} = -\boldsymbol{F_h} \tag{21}$$

$$\rho_w TA_t \boldsymbol{S_{pz}} = -\boldsymbol{F_h} \tag{22}$$

$$\begin{aligned} \boldsymbol{S_{pz}} &= \frac{-\boldsymbol{F_h}}{\rho_w TA_t} V_i \\ &= -\frac{1}{2}\left|\sqrt{\frac{2}{2-(C_D+C_L)}}\boldsymbol{U_c} - \boldsymbol{v}\right|^2 \frac{C_D \boldsymbol{i_D} + C_L \boldsymbol{i_L}}{T} V_i \end{aligned} \tag{23}$$

2.5. Coupling algorithm

The two solvers in the present study, *i.e.*, Code_Aster and OpenFOAM, are written in an object-oriented manner and open source. Hereby, it is feasible to couple the two solvers to study the FSI problem. The coupling is achieved through our in-house module, which allows information exchange between the two solvers. The two-way coupling algorithm is illustrated in Fig. 9, and the main procedures are:

(1) At the beginning of simulations, the two solvers load the physical parameters from a dictionary file and initialise the model according to the configuration of nets. In the initialisation, porous

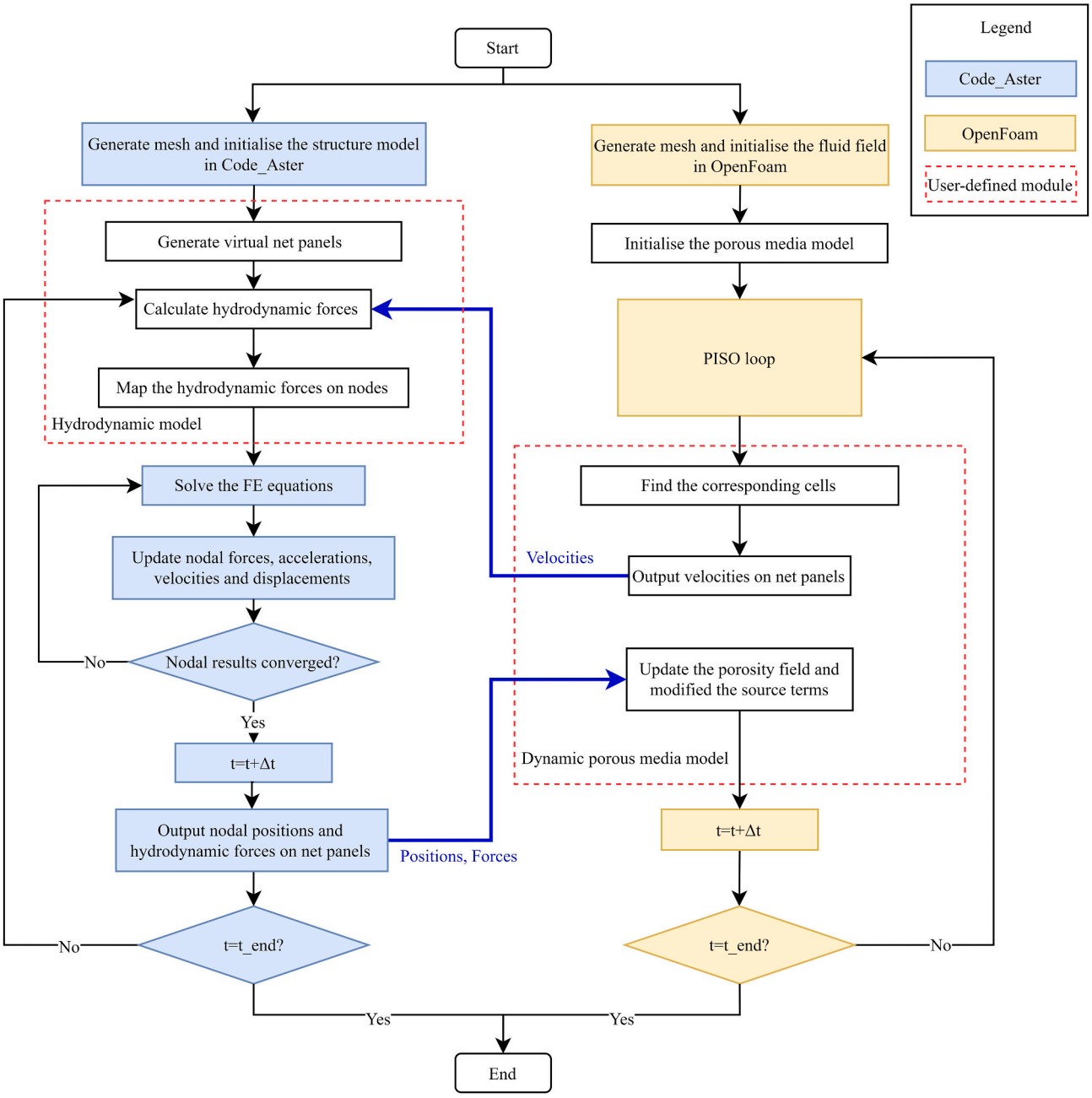

Fig. 9. Flow chart showing the coupling algorithm.

zones are created in the fluid solver, and virtual net panels are created in the structural solver.

(2) The fluid solver solves the flow field using the PISO algorithm.

(3) The velocities in porous zones are extracted from the fluid solver and corrected using Eq.(10).

(4) The Screen model employs the corrected velocities to calculate the hydrodynamic forces on nets.

(5) The hydrodynamic forces on nets are mapped onto the corresponding structural nodes.

(6) Based on the received hydrodynamic forces, the structural solver calculates the position of each structural node using the HHT-α algorithm.

(7) The DPM model updates the shapes of porous zones based on the topological method in Section 2.4.1 and the value of S_{pz} in fluid cells using Eq.(23).

(8) The fluid solver calculates the flow field with the newly updated porous zones as in Step (2). Hereby, a full loop to solve the FSI problem is built.

2.6. Comments on the proposed coupling algorithm

The present coupling procedure is conceptually similar to the IBM (Pepona and Favier, 2016; Griffith and Patankar, 2020; Wang et al., 2017) for moving structures, but it employs a different way (see Eq. (23)) to convert the fluid pressure into a structural load. This is because the conventional IBM for impermeable solid cannot be used for the highly permeable nets. In the present coupling algorithm, the DPM model is developed to handle the porous nets in a computationally affordable way. Although the names of the additional source term S_{pz} varies in different publications (O'Neill, 2006; Patursson et al., 2010; Martin et al., 2020), the methods are conceptually similar. Essentially,

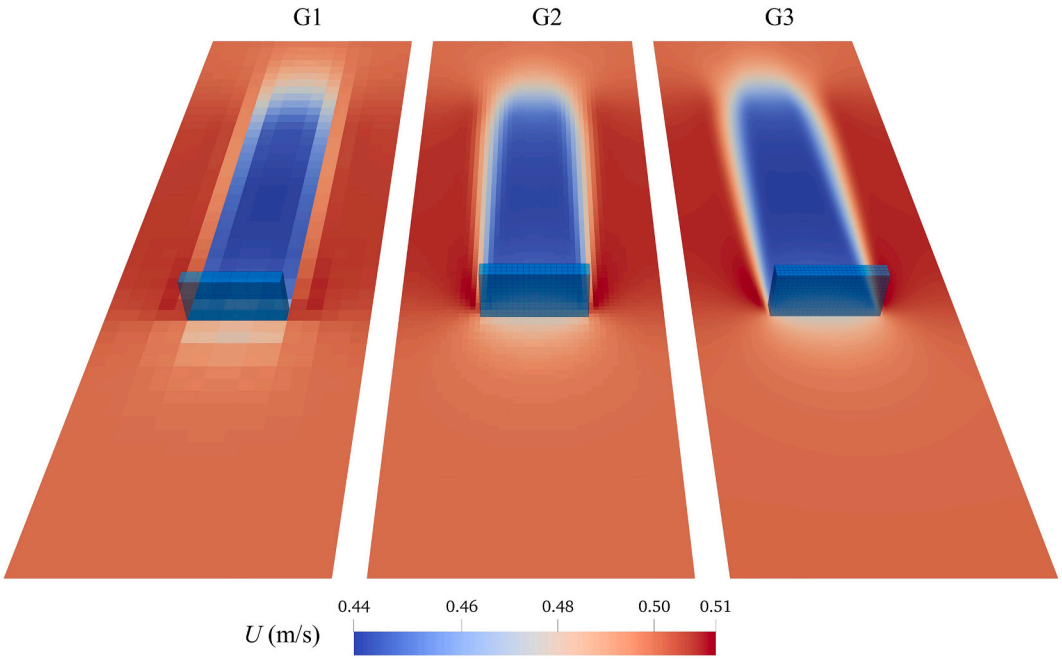

Fig. 10. Mesh convergence study with different $T/\Delta x$.

Table 1
Results of convergence study for a fixed net panel in steady flow when $\theta = 0°$.

Grid	Cells	$T/\Delta x$	F_D	Deviation	u^*	Deviation
G1	20 352	1	35.602 N	7.70%	0.4344	0.73%
G2	560 952	3	33.431 N	1.14%	0.4381	0.11%
G3	2 638 494	5	33.056 N	–	0.4376	–

u*: flow velocity at the red circle in Fig. 11 (a).

$\boldsymbol{S_{pz}}$ is added to the momentum equations to account for the resistance of nets. Compared to Martin et al. (2020), the present coupling algorithm fulfils the law of momentum conservation which is a fundamental principle for reliable results. In comparison to the coupling algorithm using "force balance" concept (Bi et al., 2014b; Yao et al., 2016), the present time-stepping algorithm is more advanced and is applicable to both steady and unsteady flow conditions.

Different from the previous studies (Patursson et al., 2010; Bi et al., 2014a; Chen and Christensen, 2016) where the hydrodynamic forces were calculated using Morison models, the present algorithm employs the advanced Screen models to calculate the hydrodynamic forces. According to Cheng et al. (2020), the advanced Screen models can improve the accuracy of the environmental load, which is a basis for structural responses. Moreover, compared to the approach proposed by Patursson et al. (2010) and Chen and Christensen (2016), the new algorithm properly removes the additional process for fitting the porous coefficients, which implicitly includes the velocity correction. Because considerable experimental and theoretical studies on Screen models are already published (Fridman, 1973; Aarsnes et al., 1990; Løland, 1991; Balash et al., 2009; Kristiansen and Faltinsen, 2012; Bi et al., 2018), the hydrodynamic force coefficients C_D and C_L can be directly obtained from these published articles and applied in the present algorithm. Thus, the present algorithm can simplify the procedures for the model preparation and improve the accuracy of the structural responses.

3. Validation of the numerical method

In this section, series of experiments conducted by Patursson et al. (2010), Bi et al. (2014a), and full-scale sea trials conducted by Gansel et al. (2018) are taken as references for the validation study of the present coupling algorithm. A convergence study is performed at first to determine the appropriate spatial resolution for the simulations. Then, the flow velocities behind a fixed net panel under several inflow angles (θ) are compared with the experimental data by Patursson et al. (2010). After that, the deformations of two flexible net panels are compared with the experimental data by Bi et al. (2014a). Finally, the drag forces on the full-scale fish cage under different flow velocities are calculated and compared to the sea trials by Gansel et al. (2018).

3.1. Convergence studies

In the present study, hexahedral orthogonal grids are employed to discretise the fluid domain in the fluid solver. Although the thickness of the porous zone has a negligible effect on the simulations results (Patursson et al., 2010), the number of cells across the porous zone might affect the results (Chen and Christensen, 2016). Thus, a grid convergence study should be performed to determine $T/\Delta x$, where T is the thickness of the porous zone, and Δx is the cell size. The grid convergence study is carried out with three sets of grids (G1-G3) for the cases in Patursson et al. (2010). The detailed setup of the numerical model is given later in Section 3.2, and the results for the convergence study are shown in Fig. 10 and Table 1. The deviation in Table 1 is calculated based on the finest grid resolution (G3).

As shown in Table 1, G2 can achieve very close results in comparison to the finest grid regarding both the drag force $\boldsymbol{F_D}$ and flow velocity in the wake. However, G1 overpredicts $\boldsymbol{F_D}$ by 7.7% compared to the finest grid. As the three sets of grids use the same hydrodynamic force coefficients from Patursson et al. (2010) to calculate the drag force, the discrepancies of $\boldsymbol{F_D}$ in numerical results by the three sets of grids are only induced by the differences of $\boldsymbol{U_c}$. The large discrepancies between G1 and G3 indicate that $T/\Delta x$=1 might be too coarse to solve the fluid field around the net. As for the flow velocities in the wake, which is extracted from the red spot in Fig. 11, discrepancies of the results from G1-G3 are less than 1%. Therefore, it can conclude that the numerical simulation is converged when $T/\Delta x \geq 3$. For the subsequent simulations, $T/\Delta x = 3$ is chosen for the spatial resolution in the fluid solver. Regarding the structural mesh, the convergence study by Cheng et al. (2020) has demonstrated that the results using different numbers of elements have a maximum 1.69% deviation. Thus, the structural mesh is generated by

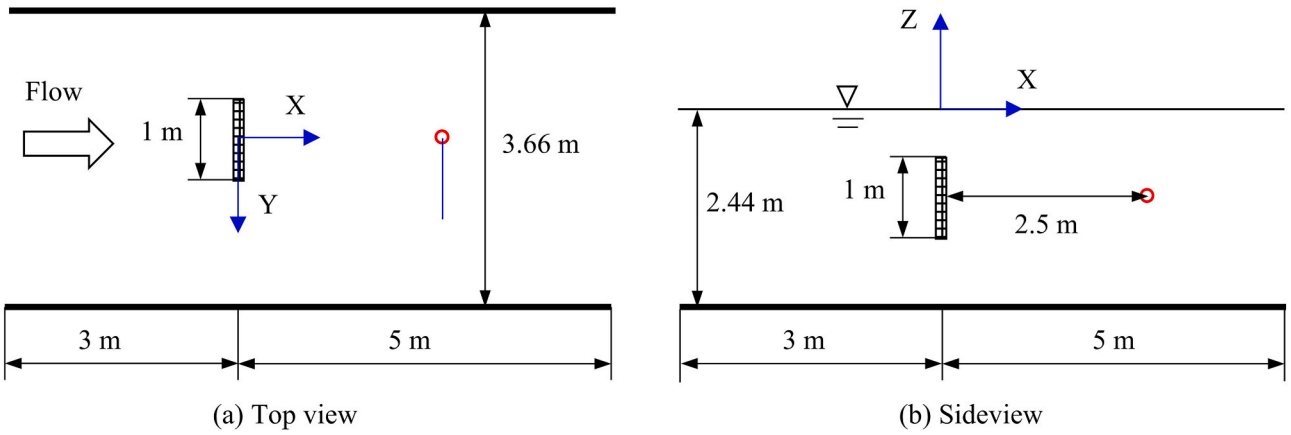

Fig. 11. Sketch of the fluid domain for the reproduction of the experiment by Patursson et al. (2010) Top view is shown on the left, side view is shown on the right. The flow velocities in the wake are measured at the red circle. (For interpretation of the references to colour in this figure legend, the reader is referred to the Web version of this article.)

Table 2
Deviations for the flow reduction factor between numerical simulations and experimental data by Patursson et al. (2010) when $\boldsymbol{U}_{-\infty} = 0.5$ m/s.

	θ	0°	15°	30°	45°	60°	75°
Experiment	C_D	0.258	0.243	0.210	0.157	0.106	0.077
	C_L	0	0.037	0.064	0.075	0.069	0.035
	r_u	0.889	0.886	0.889	0.885	0.865	0.738
Simulation	r_u	0.876	0.880	0.882	0.896	0.899	0.902
	Deviations	−1.45%	−0.79%	−0.45%	1.24%	3.70%	22.67%

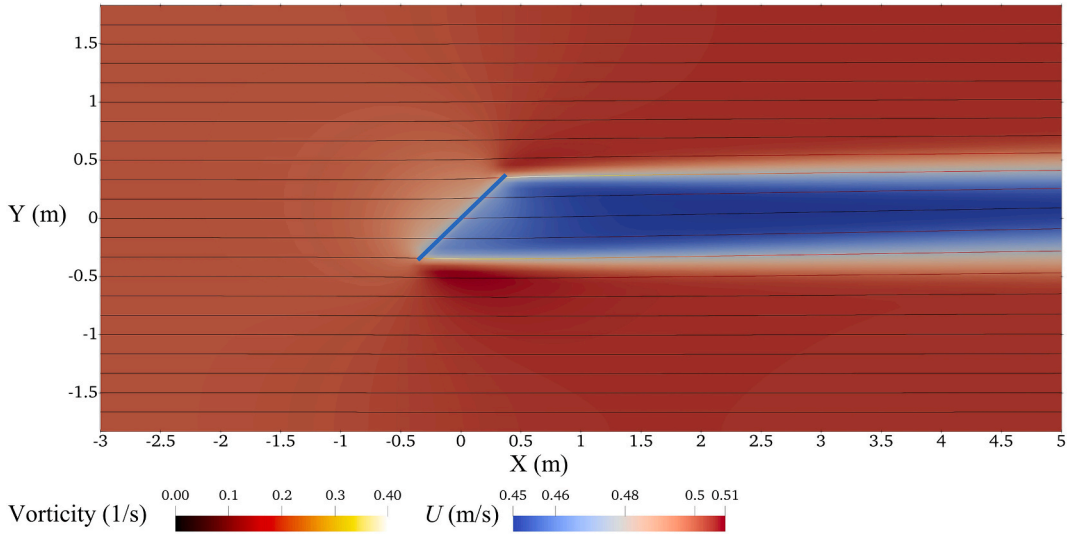

Fig. 12. The velocity contour from the present numerical model on the X–Y plane at Z = −1.22 m when $\theta = 45°$ and $\boldsymbol{U}_{-\infty} = 0.5$ m/s. The blue line represents the net panel. (For interpretation of the references to colour in this figure legend, the reader is referred to the Web version of this article.)

mainly considering the calculational domains and computational costs.

The time-step convergence study is also performed for the nets in pure currents. The conclusion is similar to Cheng et al. (2020), where four time steps, *i.e.* 0.02s, 0.05s, 0.1s and 0.2s, were applied. Since the simulations are calculated under pure current conditions without any oscillating loads, the above time steps have negligible influences on the final results. Thus, a time step 0.1 s is selected for all the subsequent simulations by considering the Courant–Friedrichs–Lewy (CFL) number. In the following simulations, the maximum CFL number is 0.3.

3.2. Fixed net panel

3.2.1. Case setup

The first validation is based on the experiments by Patursson et al. (2010). In the experiments, a net panel was fixed to a square frame and towed under various inflow angles and velocities. The net panel was made of a 1 m × 1 m knotless nylon material with $d_{w0} = 2.8$ mm, $L = 29$ mm and $Sn = 0.2$. The purpose of this validation is to test whether the flow field behind a net panel can be correctly predicted. The flow reduction factor r_u is used in this validation to indicate the accuracy of the numerical simulations. r_u is calculated as the ratio between the velocity at the probe (the red circle in Fig. 11) and the undisturbed

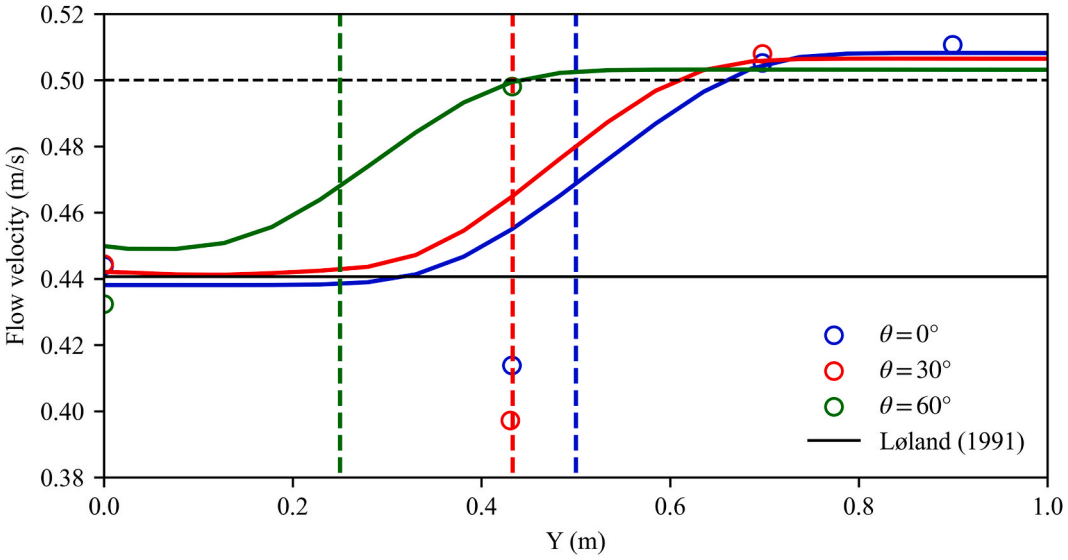

Fig. 13. Flow velocity profiles from numerical simulations. The vertical dashed lines show the position of the vertical frame for the different inflow angles.

incoming velocity.

The sketch of the simulation domain is shown in Fig. 11. In the numerical model, G3 is chosen for the spatial resolution in the fluid solver, and 220 elements with $\lambda = 3.45$ are used to represent the net in the structural solver. For the boundary conditions in the fluid solver, $\boldsymbol{u} =$ 0.5 m/s, k =3.75 × 10^{-5} m^2s^{-2} and ε=2.5 × 10^{-7} m^2s^{-3} are set as fixed values on the inlet boundary according to the data provided by Patursson et al. (2010). In the structural model, the nodes on the four edges are fixed to represent the setup in the experiments. The square frame which was used to support the net is not modelled in the present simulations. The hydrodynamic forces on net panels are calculated using the force coefficients in Table 2, which are derived based on the experimental data from Patursson et al. (2010).

3.2.2. *Flow patterns behind the single net panel*

Fig. 12 presents the flow velocity field and the streamlines on the X–Y plane at Z = −1.22 m when $\theta = 45°$ and $\boldsymbol{U}_{-\infty} = 0.5$ m/s. The wake region behind the net panel is visible and has approximately the same width as the projected width of the net panel. The magnitude of the flow velocity in the wake is smaller than $\boldsymbol{U}_{-\infty}$. Since the drag force on the net can cause a loss of momentum on the fluid, it is reasonable to observe a flow velocity reduction in the wake. Besides the velocity reduction, the flow is also deflected by the net panel, shown as the slightly bent streamlines in Fig. 12. When $\theta = 45°$, the fluid flow can cause a lift force on the net. The lift force can, in turn, lead the flow to an opposite direction according to Newton's third law. This flow deflection is also reported by Reynolds (1969). Therefore, it can conclude that the existence of the net can reduce the flow velocity and change the flow direction.

The turbulence model is necessary for simulating the flow field in the wake region. According to Laws and Livesey (1978), the net panel in the present study works like a turbulence-suppressing screen in a wind tunnel, which can produce a steady and uniform flow. Thus, it is expected to observe a steady and uniform flow behind the net panel in Fig. 12. According to the numerical results by Martin et al. (2020) and Chen and Christensen (2017), the flow field in the wake region showed a stripe pattern when the turbulence model was absent. The stripe pattern indicates that the flow field in the wake has a sharp velocity gradient and high nonuniformity. As a turbulence model is employed in the present study, the turbulent diffusion causes momentum exchange in-between the layers with different velocities. The momentum exchanging reduces the velocity variation. Thus, the turbulence model can remove the unphysical sharp velocity gradient and produce a uniform wake flow. Moreover, the uniform flow is theoretically better than the stripe-pattern flow for calculating the hydrodynamic forces on nets. Because the hydrodynamic forces are calculated using the flow velocity extracted from the fluid solver, the stripe-pattern flow can cause a large-variation load. Hereby, dynamic responses of the whole structure may be unstable and unreliable without any turbulence model. An example of unstable numerical results is reported by Chen and Christensen (2017). Therefore, it is suggested to add a turbulence model in simulations in order to achieve reasonable and stable solutions.

3.2.3. *Flow velocity profiles behind the net panel*

Fig. 13 shows the flow velocity profiles along the blue line in Fig. 11 from the numerical simulations with different inflow angles. The circles in this figure represent the experimental measurements provided by Patursson et al. (2010). According to the flow velocity profiles, the velocity gradually decreases from the flank of the towing tank to the centre plane of the towing tank. Near the flank of the towing tank, the flow velocity is approximately 3% higher than $\boldsymbol{U}_{-\infty}$. This velocity increment is the result of mass conservation. Around the centre plane of the towing tank, the flow velocity is reduced due to the loss of momentum. In general, the velocity profiles from the numerical simulations agree well with the experimental measurements except for the two measurements at Y = 0.43 m. When $\theta = 0°$ and 30°, the velocity probe is located in the wake region generated by the frame. As the frame is not modelled in the numerical simulation, it is reasonable to observe the discrepancy of the velocities at Y = 0.43 m when $\theta = 0°$ and 30°. The engineering approach proposed by Løland (1991) is shown in Fig. 13 for comparison. It indicates that the engineering approach fits well with the experimental measurements at the centre plane of the towing tank when $\theta < 60°$.

3.2.4. *Flow reduction factor*

In general, the flow reduction factor (r_u) can be accurately predicted by the present model. As shown in Table 2, the differences between the predicted r_u and the experimental results are within 1.5% when $\theta < 60°$. The large deviation is only seen when the inflow angle $\theta = 75°$. For the cases when $\theta > 60°$, the large deviation can be explained mainly by the two reasons. First, the experimental data might have errors when $\theta >$ 60° by using the experimental setup in Patursson et al. (2010). As reported by Tang et al. (2018, 2019), a special-designed experiment together with a streamlined frame is essential for measuring the drag force when $\theta > 60°$. If the flawed force coefficients are employed by the present FSI method, the hydrodynamic forces and the flow field can be inaccurate. Second, the rigid frame is not modelled in the present study due to the insufficient descriptions in Patursson et al. (2010). As shown

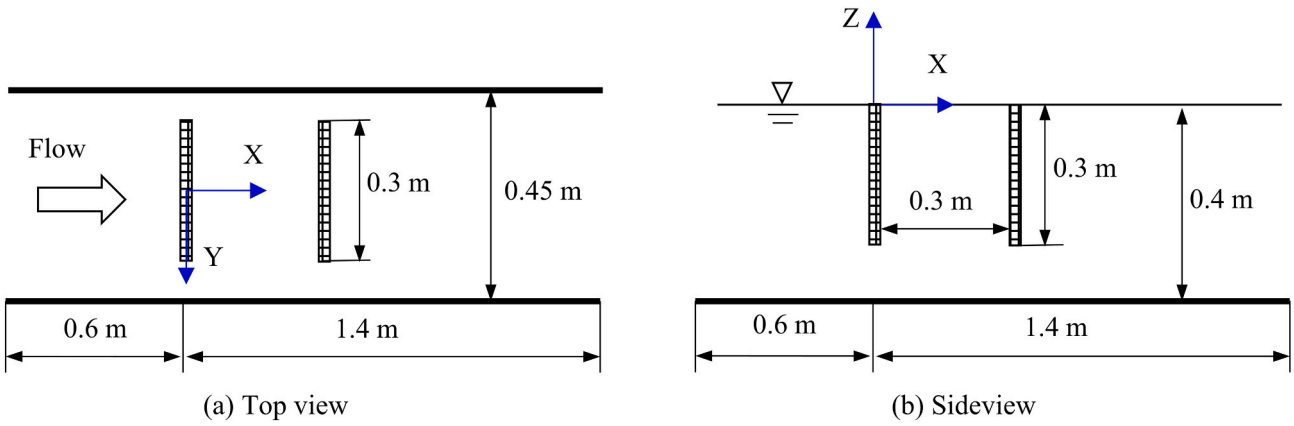

Fig. 14. Sketch of the simulation domain for the reproduction of the experiment by Bi et al. (2014a). The top view is shown on the left, and the side view is shown on the right.

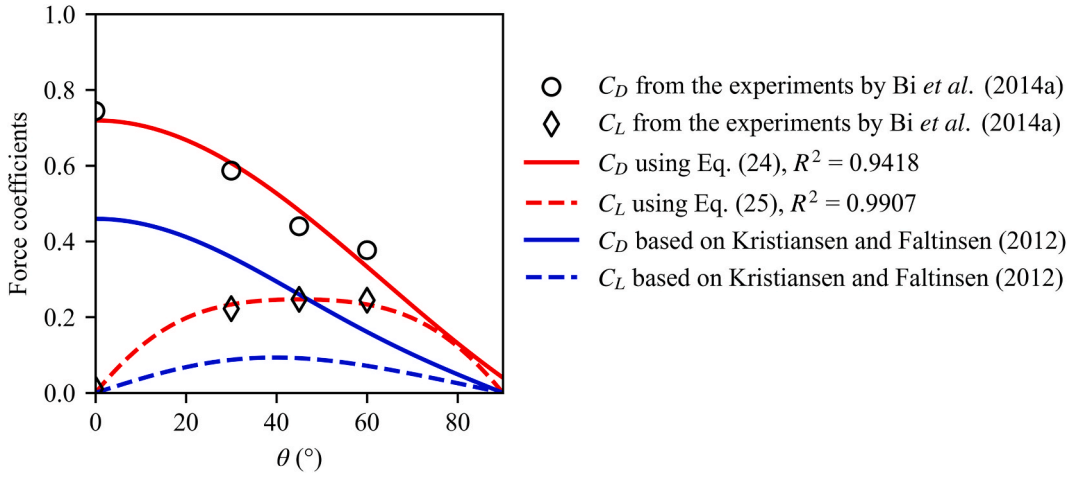

Fig. 15. The force coefficients from experimental measurements by Bi et al. (2014a).

in Fig. 13, if the probes are located in the wake region generated by the frame, the measured velocity will be reduced significantly. When $\theta = 75°$, the probe (the red circle in Fig. 11) is affected by the frame. Thus, the measured velocity is reduced significantly. For these two reasons, it is expected to observe the large deviations when $\theta > 60°$.

3.3. Two flexible net panels

3.3.1. Case setup

The second validation is performed based on the experiments by Bi et al. (2014a), where two flexible net panels are under the action of steady currents. The purpose of this validation is to test whether the present coupling algorithm can accurately predict the deformations of flexible nets and the downstream flow velocity. In the experiment, the tops of the two net panels were fixed on bars just below the free surface. On the bottom of the net panels, steel bars with a density of 8 610 kg/m^3 were mounted as sinkers. The length and diameter of the steel bars were 0.3 m and 6 mm, respectively. Each net panel is made of a 0.3 m × 0.3 m knotless polyethylene net with $d_{w0} = 2.6$ mm, $L = 20$ mm and $Sn = 0.26$.

The sketch of the simulation domain is presented in Fig. 14. In the present numerical model, 2 872 800 cells with $T/\Delta x = 3$ are used for the spatial resolution in the fluid solver, 120 elements with $\lambda = 3.0$ are used in the structural solver to represent the two net panels. According to the experiments (Bi et al., 2014a), the turbulence intensity is 4.37% when $\boldsymbol{U}_{-\infty} = 0.226$ m/s. Thus, $\boldsymbol{u} = 0.226$ m/s, $k = 1.46 \times 10^{-4}$ m^{2}s^{-2}, $\varepsilon = 2.88 \times 10^{-5}$ m^{2}s^{-3} are set as the inlet boundary conditions in the fluid solver.

In the structural model, nodes on the top of the net panels are fixed to represent the setup in the experiments. Regarding the hydrodynamic forces, C_D and C_L are acquired by fitting the measured data from Bi et al. (2014a). The two force coefficients are expressed as follows:

$$\begin{cases} C_D = 0.04 + 0.4921\cos\theta + 0.1873\cos^2\theta \\ C_L = 0.4159\sin 2\theta - 0.169\sin^2 2\theta \end{cases} \tag{24}$$

Fig. 15 shows the force coefficients of the fixed flat net panel based on experimental measurements by Bi et al. (2014a). In the experiments, the drag and lift forces on the net panel were measured under four inflow angles when $\boldsymbol{U}_{-\infty} = 0.170$ m/s. Because both the fixed and flexible net panels were made of the same net, the force coefficients of the fixed net panel can be applied to the two flexible net panels. As shown in Fig. 15, the force coefficients in Eq.(24) well agree with the experimental data. However, the force coefficients which are derived based on a finite net panel in an infinite flow field by Kristiansen and Faltinsen (2012) are significantly smaller than those based on the experiments by Bi et al. (2014a). The expressions of the later force coefficients are given in Section 3.4 (Eqs. (25)-(27)). The large discrepancies can be explained by the two following reasons. First, the forces on the net panel were measured in a flume tank with a limited width by Bi et al. (2014a). The ratio between the width of the net panel and the width of the flume tank is = 0.67. As explained in Section 2.2, the force coefficients should be measured in the ideal condition where a finite net panel is placed in an infinite flow field. When the width of the flume tank is insufficient, the existence of the net panel can speed up the flow velocity on the net due

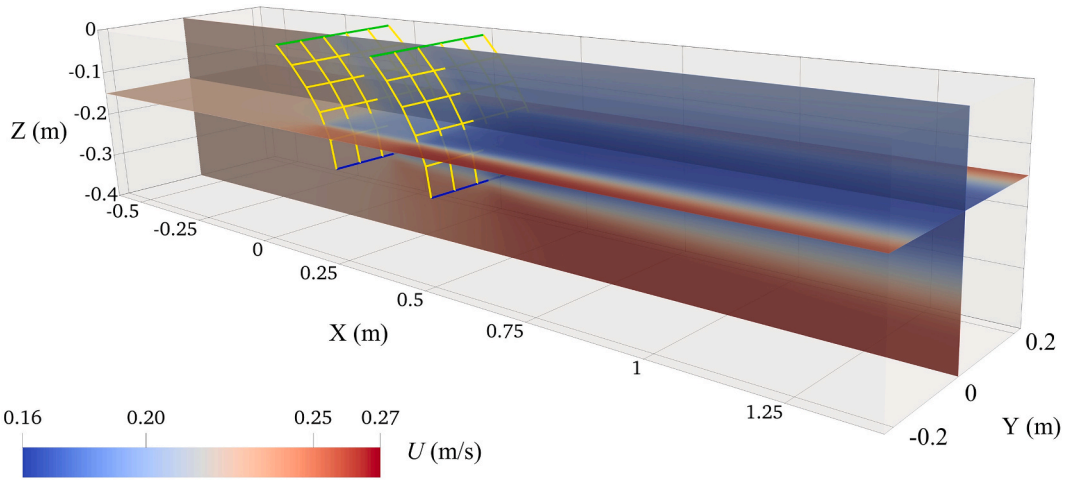

Fig. 16. Deformation of the two flexible net panels when $\boldsymbol{U}_{-\infty} = 0.226$ m/s. The yellow lines represent the nets. The green lines represent fixed parts of the nets. The blue lines represent the steel bars attached to the net bottom. (For interpretation of the references to colour in this figure legend, the reader is referred to the Web version of this article.)

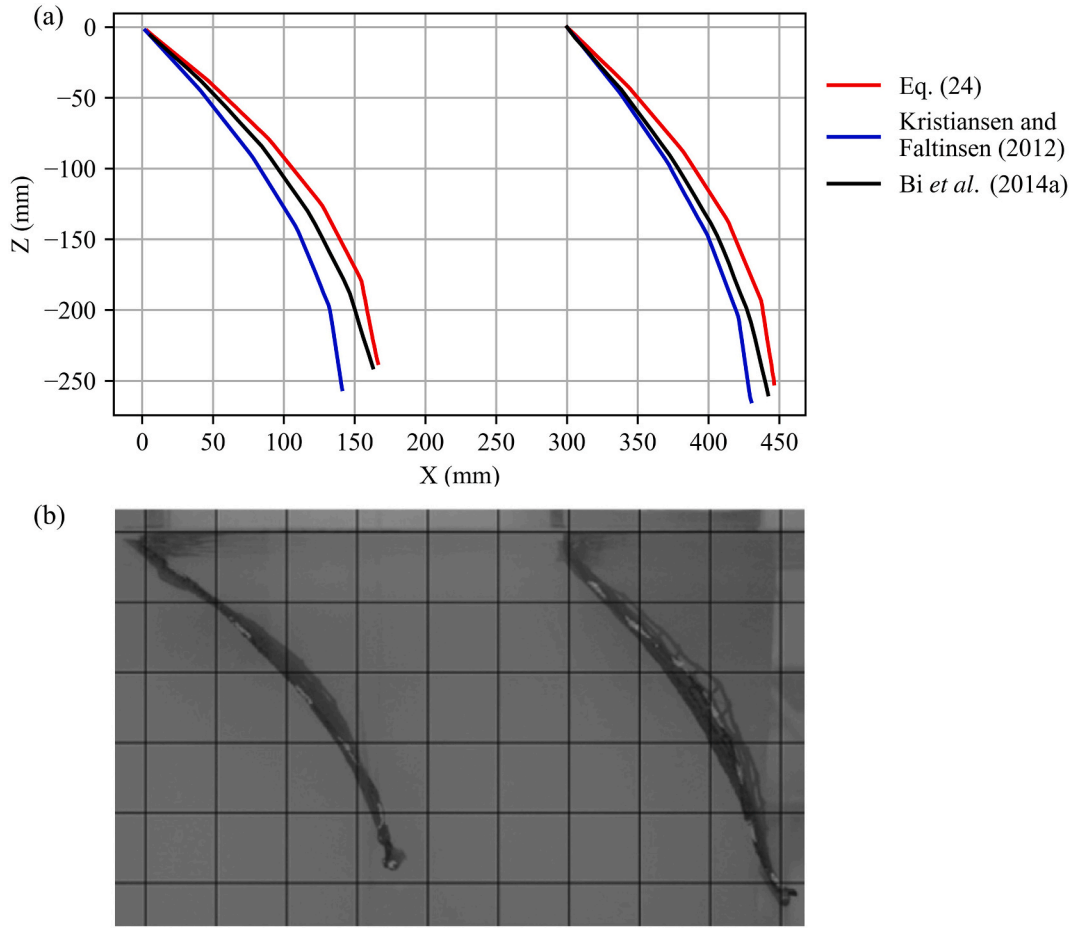

Fig. 17. Deformations of two flexible net panels when $\boldsymbol{U}_{-\infty} = 0.226$ m/s. (a) Numerical simulation results: The red lines use the force coefficients in Eq. (24); The blue lines use the force coefficients based on Kristiansen and Faltinsen (2012), *i.e.*, Eqs. 25–27; The black lines are from Bi et al. (2014a), where the hydrodynamic forces are calculated using the Morison model, and the nets are modelled using a lumped-mass method. (b) Experimental results. (For interpretation of the references to colour in this figure legend, the reader is referred to the Web version of this article.)

to the mass conservation. The speed-up velocity can cause an increment in the hydrodynamic forces. Hereby, the forces coefficients in the experiments by Bi et al. (2014a) are higher than the force coefficients proposed by Kristiansen and Faltinsen (2012). Second, the differences in materials and geometrical parameters of the nets can also contribute to the discrepancy of the force coefficients. This discrepancy can cause different structural responses in numerical simulations, which are revealed in Fig. 17(a).

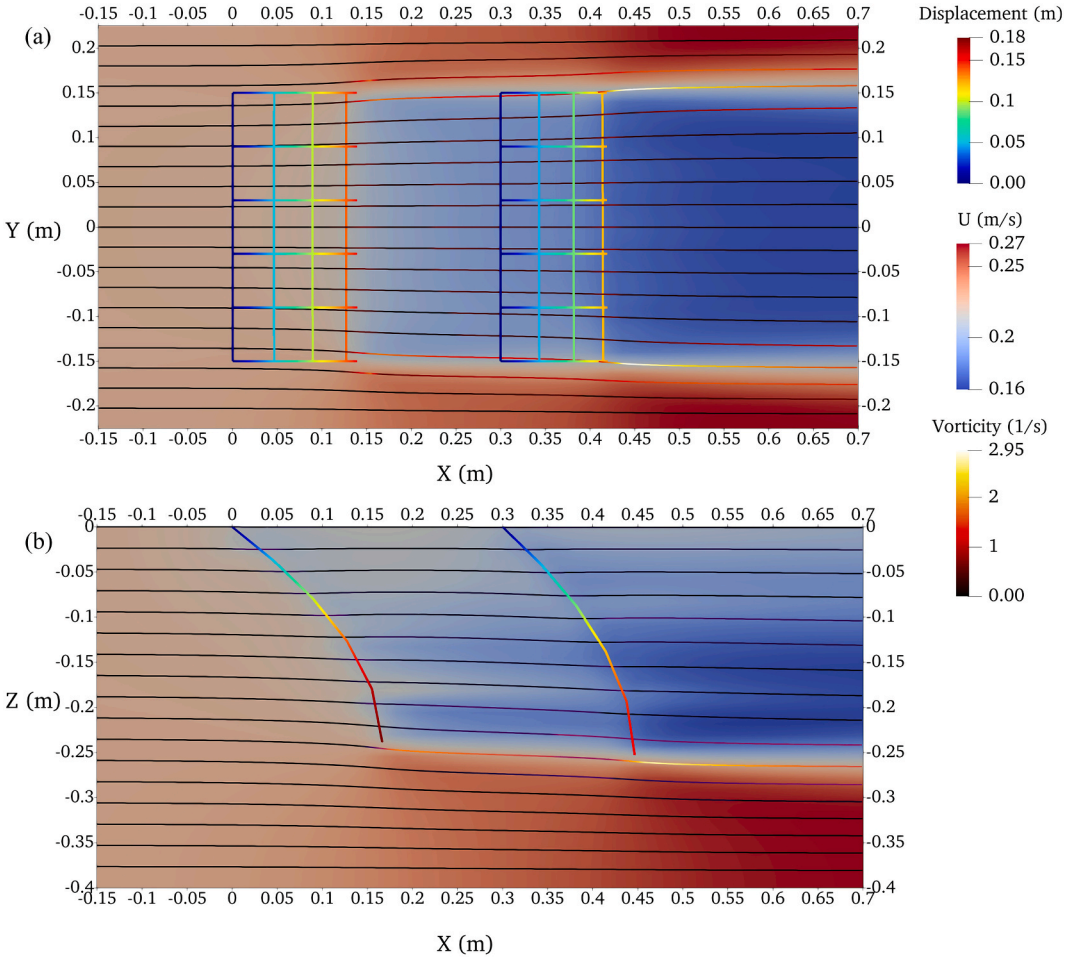

Fig. 18. Flow velocity field around the flexible net panels. (a) Contours on the horizontal plane Z = −0.15 m; (b) Contours on the vertical plane Y = 0 m.

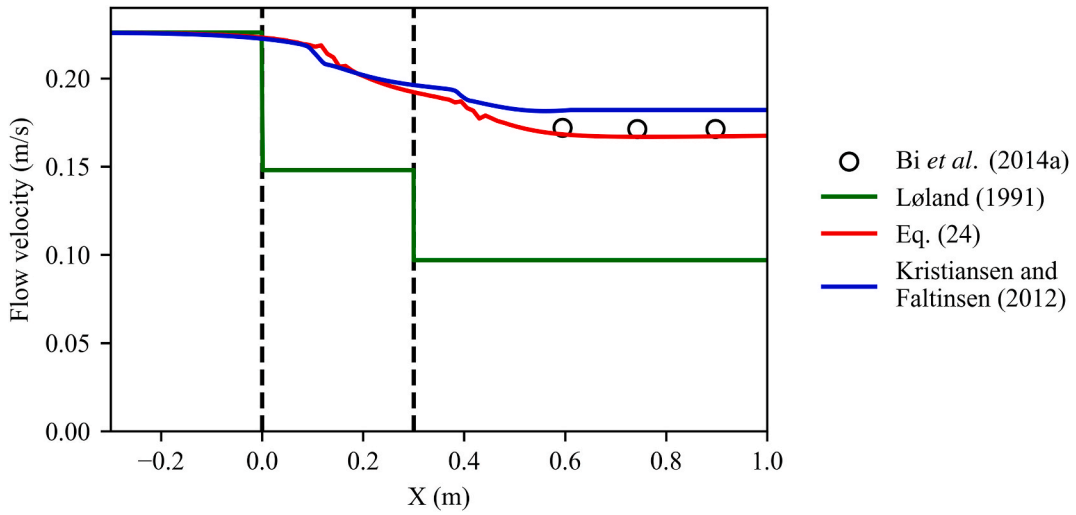

Fig. 19. Flow velocity along the line Y = 0 m on the plane Z = −0.15 m. The two vertical dash lines show the initial positions of the net panels.

3.3.2. *Structural deformation*

As shown in Fig. 16, the presented numerical model can reproduce the experimental results (Bi et al., 2014a) in the three-dimensional domain. The flow reduction behind the net panels can be observed. The results at two planes, *i.e.* Y = 0 m and Z = −0.15 m, will be used to compare with the numerical results by Kristiansen and Faltinsen (2012) as well as the numerical and experimental results by Bi et al. (2014a) in the subsequent discussion.

Fig. 17 (a) shows the deformations of the two flexible net panels obtained from the present numerical simulation, Kristiansen and Faltinsen (2012) and Bi et al. (2014a). Fig. 17 (b) shows the corresponding experimental measurements reported by Bi et al. (2014a). Compared to

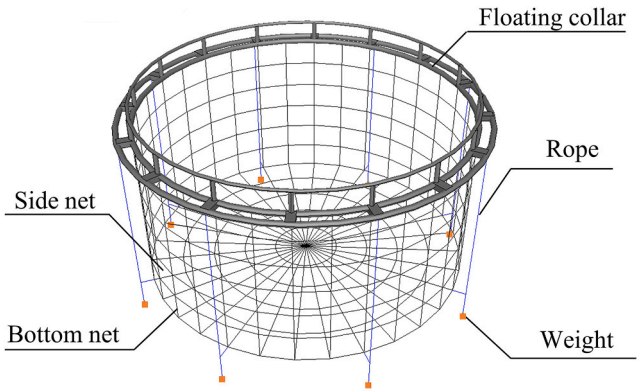

Fig. 20. Illustration of the fish cage in the sea trials by Gansel et al. (2018).

Table 3
The parameter of the full-scale fish cage in the sea trials and numerical simulations.

	Full-scale model	Numerical model
Cage diameter (m)	12	12
Cage height (m)	6	6
Submerged weight (Kg)	35 × 8	35 × 8
Bottom ring (kg/m)	0.5	0.5
Twines Young's modulus (MPa)	400	400
Twines density (kg/m^3)	1140	1140
Net half mesh size (mm)	15	1000*
Net twine diameter (mm)	2	16.33*
Solidity	0.27	0.27

* The net half mesh size in the numerical model is larger than the Full-scale model because of the mesh grouping method proposed by Cheng et al. (2020). The net twine diameter in the table refers to the structural diameter (d_{ws}). For the elastic diameter (d_{we}) and the hydrodynamic diameter (d_{wh}), please refer to Cheng et al. (2020).

the numerical results using the force coefficients based on Kristiansen and Faltinsen (2012), the present results using Eq. (24) show a better agreement with the experimental results (Fig. 17 (b)). The better agreement indicates that: (1) the numerical results are sensitive to the force coefficients; (2) the numerical simulation should use the force coefficients as accordant to the experiments as possible. Although the hydrodynamic force model proposed by Kristiansen and Faltinsen (2012) has been tested in many studies and achieved acceptable results (Yao et al., 2016; Martin et al., 2020), the mismatched force coefficients make the simulations fail to predict the deformations of the net panels correctly. Compared to the numerical results by Bi et al. (2014a), the results by using Eq. (24) shows only a small discrepancy. This small discrepancy might come from the differences in coupling algorithms, structural model and hydrodynamic force model.

3.3.3. *Flow patterns behind the two net panels*

Fig. 18 shows the flow field around the two flexible net panels using the present coupling algorithm together with force coefficients in Eq. (24). As observed, the flow velocity below and in the flanks of the net panels increases by 20% compared to $\boldsymbol{U}_{-\infty}$. The velocity increment is relatively large compared to that from the experiments by Patursson et al. (2010), where the ratio between the width of the net panel and the width of the flume tank is = 0.27, and the flow velocity in the flanks of

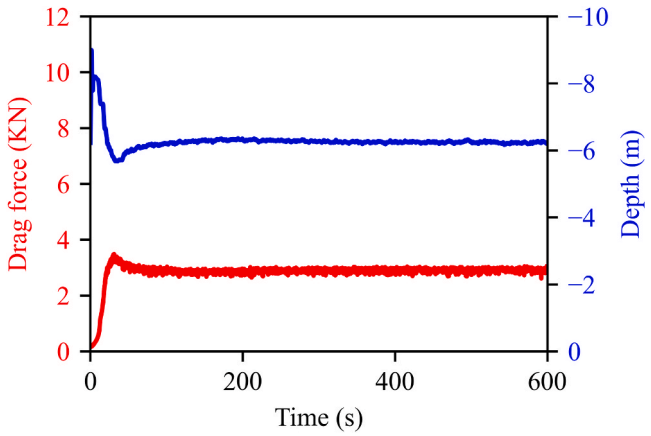

Fig. 22. Time series of the drag force on the fish cage and the depth of bottom nets from the numerical results when the towing speed is 0.509 m/s.

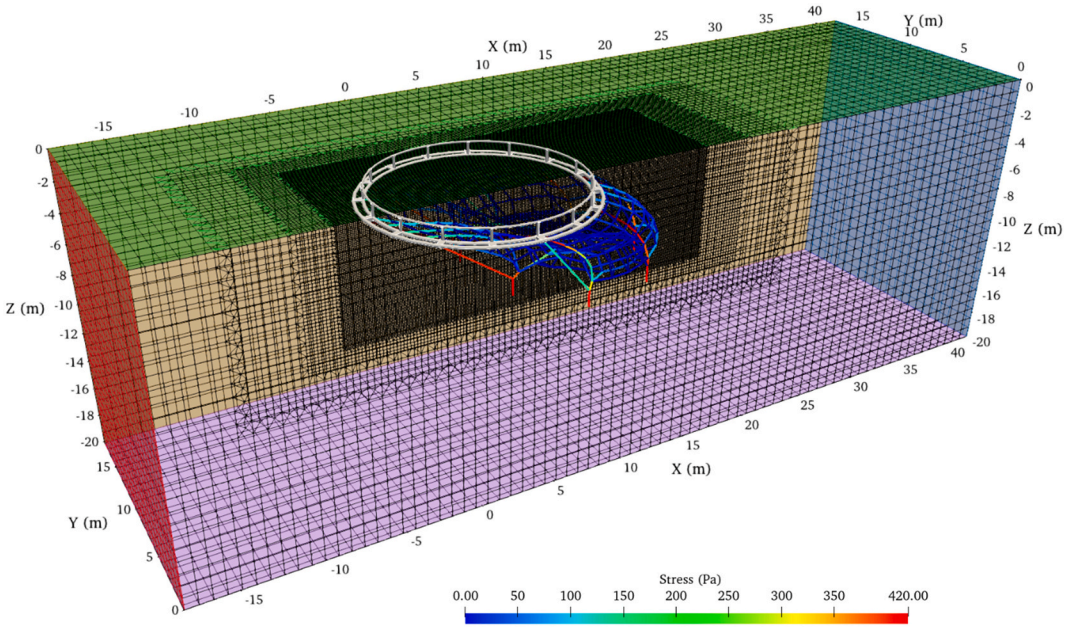

Fig. 21. The computational grid in the fluid solver and the deformed fish cage in the structural solver. The grid is refined in the vicinity of the circular cage. The computational grid is slipped on plane Y = 0 m in order to show the structural responses.

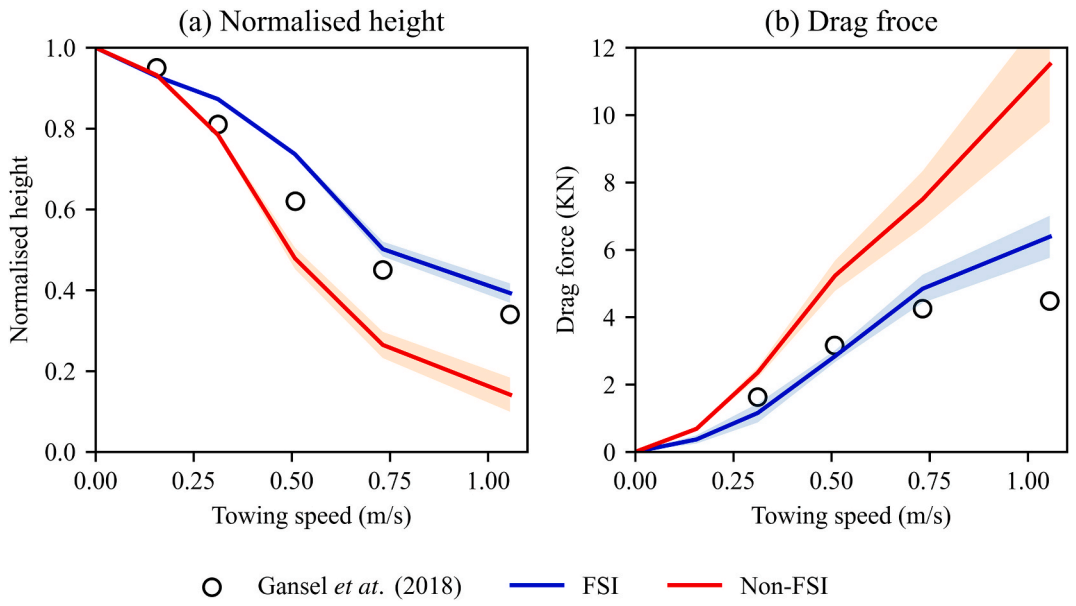

Fig. 23. Results from the two numerical methods and sea trials. The shadows show the 99.7% confidence intervals.

the net panel only increases 3%. The large velocity increment also demonstrates that the width of the flume tank in Bi et al. (2014a) is insufficient to eliminate the near-wall effects. As for the flow in the wake region, the velocity decreases 10%–15% after the flow passes each net panel. According to the streamlines in Fig. 18, the diversion of flow direction is small and only occurs near the edges of the net panels.

Besides the deformations, the flow velocity from the present numerical simulation also agrees with the experimental data well. As shown in Fig. 19, the maximum difference between the numerical results using Eq. (24) and the experimental data is only 1.4%. Because of the conservation of momentum, which is explained clearly in Section 2.4.2, it is expected that the flow velocity behind the two net panels obtained by using the force coefficients from Kristiansen and Faltinsen (2012) is higher than that by using Eq. (24). The engineering approach proposed by Løland (1991) is also included in Fig. 19 for comparison. It is observed that the flow velocity behind the two net panels by using this engineering approach is 40% smaller than the experimental data. If the smaller flow velocity is applied in the design of fish cages, the drag force on the whole fish cage can be underestimated. With the underestimated drag force, the structural design may be non-conservative.

3.4. Full-scale fish cage

3.4.1. Case setup

The third validation is performed based on a full-scaled fish cage from sea trials by Gansel et al. (2018). The purpose of this validation is to test whether the present method can accurately predict the drag force and the deformation of a full-scaled aquaculture structure. As discussed by Gansel et al. (2018), the numerical methods used in that study cannot properly predict the drag force on the full-scale fish cage because the flow field cannot be well addressed. With the present coupling algorithm, both the structural responses and the flow field are coupled and solved simultaneously. Thus, the sea trials can be properly reproduced. To the authors' knowledge, there is no published result on modelling a full-scale fish cage under different current conditions by using the FSI method. Challenges on determining the spatial resolutions and boundary conditions are raised in the numerical simulations.

An illustration of the fish cage in the seal trials by Gansel et al. (2018) is shown in Fig. 20. Eight concrete weights are attached to the floating collar and submerged to 7 m below the water surface on the outside of the net-pen with even spacing along the circumference. The main parameters of the full-scale fish cage in the sea trials and numerical simulations are given in Table 3.

In the numerical model, 2 906 299 cells with $T/\Delta x = 3$ are used in the fluid solver, 704 elements with $\lambda = 66.67$ are used in the structural solver. In order to increase the resolution around the fish cage, the grid in the fluid solver is refined in the vicinity of the fish cage. A grid convergence has been carried with the same procedure as described in Section 3.1, and the final spatial resolution is shown in Fig. 21.

In the sea trials by Gansel et al. (2018), the fish cage was towed at five different speeds in a fjord when the wave effects can be neglected. In order to minimise the effect of the bow wave caused by the boat, the fish cage is placed 350 m behind the towing boat. According to the measurements in the sea trials, the flow velocities and directions are stable over the depth of the fish cage during all tests. Thus, it is reasonable to set a uniform velocity condition at the inlet boundary in the fluid solver. Hereby, five uniform velocities, *i.e.*, 0.156 m/s, 0.312 m/s, 0.509 m/s, 0.732 m/s and 1.056 m/s, are set on the inlet boundary for each simulation. k and ε are estimated using Eq.(18) based on the assumptions that medium turbulence ($I = 5\%$) occurs in the sea trials, and the turbulence length scale L_T equals the diameter of the fish cage. In the structural model, the nodes on the floating collar are fixed to represent the setup in the sea trial. The hydrodynamic force model in the simulations follows the suggestions from Gansel et al. (2018). The force coefficients are originally proposed by Kristiansen and Faltinsen (2012) and expressed as follows:

$$\begin{cases} C_D = C_{D0}(0.9cos\theta + 0.1cos3\theta) \\ C_L = C_{L0}(sin2\theta + 0.1sin4\theta) \end{cases} \tag{25}$$

$$\begin{cases} C_{D0} = C_{cylinder}\dfrac{Sn(2-Sn)}{2(1-Sn)^2}; \\ C_{L0} = \dfrac{0.5C_{D0} - C_{L45}}{\sqrt{2}}; \\ C_{L45} = \dfrac{\pi C_{N45}}{8 + C_{N45}}; \\ C_{N45} = C_{cylinder}\dfrac{Sn}{2(1-Sn)^2}; \end{cases} \tag{26}$$

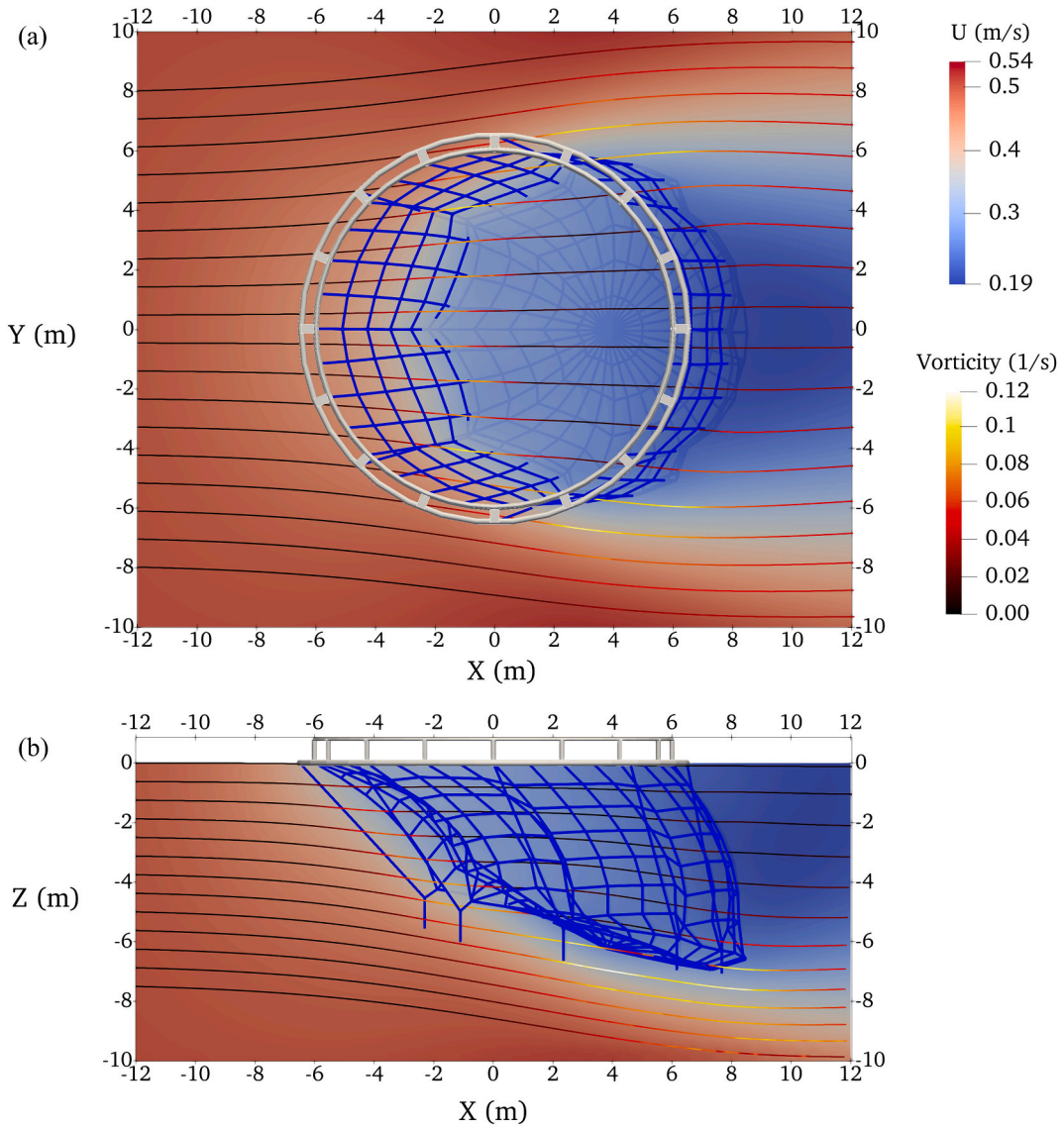

Fig. 24. Flow velocity field around the fish cage when the towing speed is 0.508 m/s. (a) Contours on the horizontal plane Z = −3 m; (b) Contours on the XZ plane Y = 0 m.

$$C_{cylinder} = 78.46675 + 254.73873log_{10}Re - 327.8864(log_{10}Re)^2$$
$$-223.64577(log_{10}Re)^3 - 87.92234(log_{10}Re)^4 + 20.00769(log_{10}Re)^5$$
$$-2.44894(log_{10}Re)^6 + 0.12479(log_{10}Re)^7; \quad (27)$$
$$Re = \frac{d_{w0}(\boldsymbol{U}_c - \boldsymbol{v})}{\nu(1 - Sn)}$$

3.4.2. Structural responses

As shown in Fig. 22, the drag force on the fish cage first increases to a peak value then decays as time increases. After 100 s, the simulation reaches equilibrium. The depth of bottom nets, defined as the depth of the lowest node on bottom nets, follows the opposite trend of the drag force. Although the simulation is performed under pure current conditions, oscillations are still observed in the present numerical results. These oscillations come from the nonlinearity of the system, which is also reported by Antonutti et al. (2018). In the present results, the standard deviation for the time-series drag force over the last 100 s is 1.8% of the mean drag force, which is smaller than that in the sea trial measurements by Gansel et al. (2018). Thus, the oscillations in the numerical results are acceptable. For the subsequent discussions, the time-averaged results over the last 100 s are used.

Fig. 23 shows the comparison of the numerical results from the FSI method and the non-FSI method along with results from sea trials. The two numerical methods use the same structural model and hydrodynamic force model, and the only difference between the two methods is the way to handle the wake effects. The FSI method models the wake effects by CFD simulations and uses the present FSI algorithm to couple the fluid and structural solvers. In contrast, the non-FSI method simplifies the wake effects by assigning flow reduction factors (r_u) onto the downstream nets without coupling with the fluid solver. In the latter method, r_u is calculated according to the engineering approach proposed by Løland (1991).

In Fig. 23 (a), the normalised height is calculated as the height of the fish cage at a given current velocity divided by the initial height of the fish cage (6 m). Since the bottom nodes of the fish cage are not in a horizontal plane, the height of the fish cage is calculated based on the average depth of the nodes on bottom nets. This averaged depth is corresponding to the data processing in the sea trials (Gansel et al., 2018). It can be observed that the height decreases with the increasing current velocity. The height of the fish cage by the non-FSI method is smaller than that of sea trial measurements, and the difference becomes

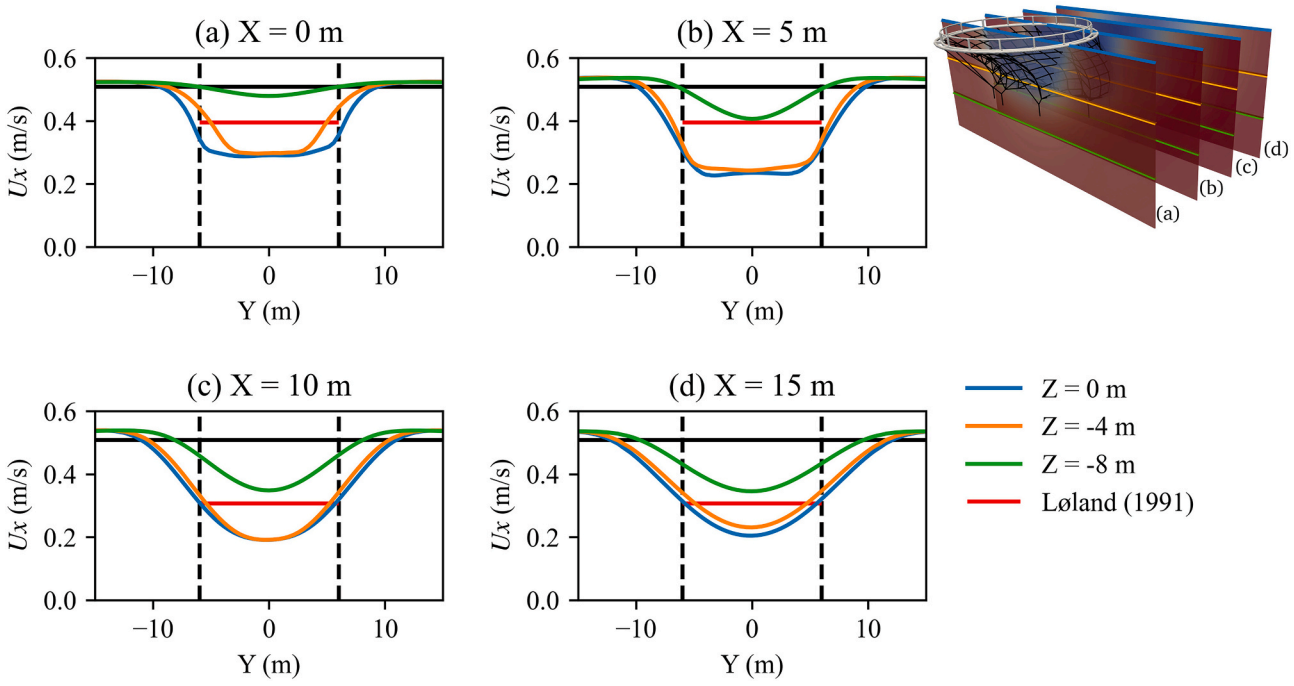

Fig. 25. Flow velocity profile on four vertical Y-Z planes, which are illustrated at the upper right corner. The undistributed flow velocity (0.508 m/s) is plotted using black lines for reference. The vertical dashed lines indicate the diameter of the fish cage.

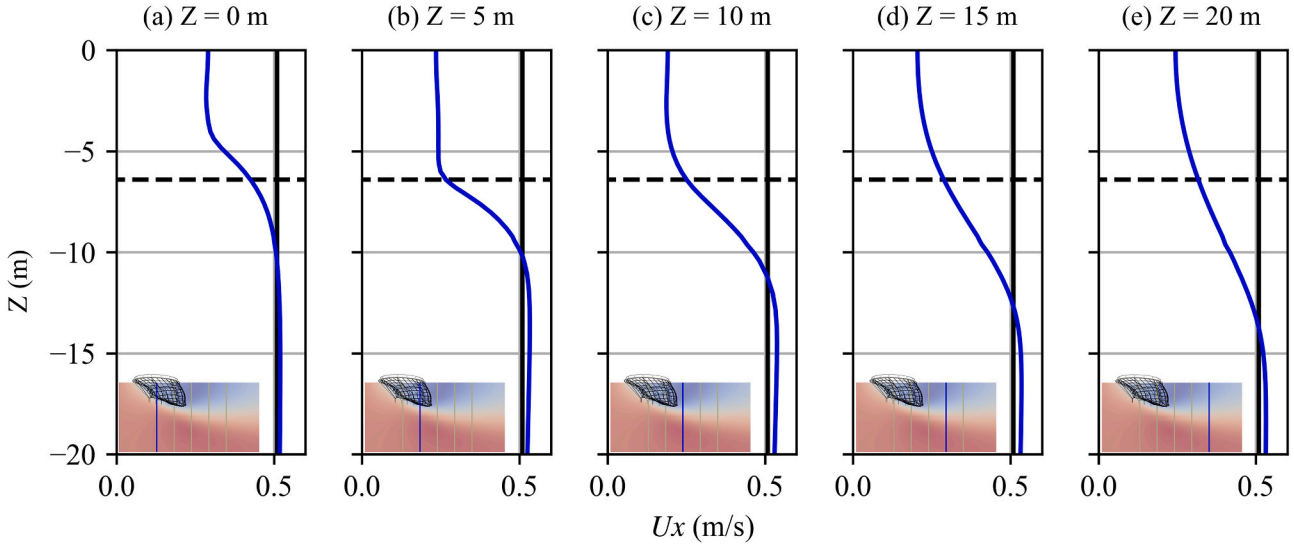

Fig. 26. Flow velocity profile on XZ plane with Y = 0. The illustration in the lower left of each subplot figure shows the location of the velocity profile. The dashed lines indicate the Z-position of the deepest node on the fish cage. The undistributed flow velocity (0.508 m/s) is plotted using black lines for reference.

distinct with the increasing current velocity.

Compared with the non-FSI method, the results from the FSI method show better agreement with the sea trials regarding the drag force. As shown in Fig. 23 (b), the drag forces by the non-FSI method are much higher than the sea trial measurements. In particular, the predicted drag force can be twice larger than the seal trials measurement when the towing speed is 1.056 m/s. In comparison, the differences between the predicted forces by the FSI method and the sea trial measurements are less than 10% when the flow velocity is smaller than 1 m/s. For the case with towing speed of 1.056 m/s, the large deviation can be explained by the two reasons: First, the measurement may have large uncertainties when the towing speed is 1.056 m/s. According to Gansel et al. (2018), the sea trial measurements were the averaged values over 10 min in the sea trial. When the fish cage was towed at 1.056 m/s, the wake behind the boat reached the fish cage after 6 min. As half of the time-series measurements were affected by the wake, the result by the sea trials at 1.056 m/s may have errors. Second, the bow wave caused by the towing boat can affect the uniformity of the incoming flow velocity at this high towing speed. As described by Gansel et al. (2018), an obvious shear flow was observed on the vertical plane Y = 0 m when the towing speed was 1.056 m/s. Since descriptions of the shear flow are insufficient, the exact boundary condition cannot be reproduced in the numerical simulation. Thus, it is reasonable to observe the large difference between the numerical simulations and the sea trial measurements when the towing speed is 1.056 m/s.

Table 4
Elapsed time for running numerical simulations.

Case	Number of elements	Number of cells	Simulation time (s)	Elapsed time (h)	
				FSI	Non-FSI
Single fixed net panel $\theta = 0°, 15°, 30°, 45°, 60°, 75°$	220	560 952	80	3.3–3.5	–
Two flexible net panels $\boldsymbol{U}_{-\infty} = 0.266$ m/s	120	202 686	60	1.1	–
Full-scale fish cage $\boldsymbol{U}_{-\infty} = 0.156$ m/s, 0.312 m/s, 0.509 m/s, 0.732 m/s, 1.056 m/s	704	2 906 299	600	18.9–19.1	6.9

3.4.3. Flow patterns behind and around the fish cage

Fig. 24 shows the flow velocity field together with the deformations of the fish cage from the present numerical simulations. As observed from this figure, the flow velocity increases approximately by 6.09% compared to the towing speed at the bottom and flanks of the fish cage. When the fluid encounters the deformed fish cage, a part of the fluid follows the guidance of curved nets. Due to the mass conservation, the flow velocity is expected to increase at the bottom and flanks of the fish cage. The flow velocity decreases up to 62.67% after the flow passes the fish cage. According to the streamlines on the horizontal plane (Fig. 24 (a)), the flow around the fish cage is almost laminar. This indicates that the TKE at the region downstream of the fish cage is insufficient to generate large vortices with a length scale of L_T. As shown in Fig. 24 (b), downward flows are observed inside and below the fish cage. These downward flows are reasonable and physical, according to Newton's Third Law. As the lift force on the font nets is upward, the lift force can, in turn, push the flow downward. Hence, the flow velocity and direction on the downstream nets are different from the upstream nets. Accordingly, it is expected that the FSI method has more accurate predictions on the responses of the full-scale fish cage than the non-FSI method, as the non-FSI method employs the engineering approach that only reduces the magnitude of flow velocity.

Fig. 25 shows the detailed velocity profiles around the fish cage from the FSI simulations. In general, the X-component flow velocity Ux is symmetric about the Y = 0 m plane, and the flow velocity reduces significantly near this symmetric plane compared to the incoming flow velocity. The width of the velocity reduction region is 1.5–2 times of the fish cage diameter, and this width increases with increasing X coordinate along the incoming flow direction. Compared to the study by Gansel et al. (2012), the widths in the present study are slightly larger than their results from the towing tank experiments, where the width is 1.1–1.4 times the cage diameter. This discrepancy of widths may come from different nets: the experiments in Gansel et al. (2012) used rigid metal nets, while the present study considers flexible nylon nets. The different net materials can make their twines have different surface roughness, and thus may cause different flow separations around the twines of nets. Consequently, the wake of the cage can have different widths. Besides, the deformation properties can also cause the discrepancy of wake widths. The deformed nets can guide part of the flow to the bottom. Hence, the fluid at the region downstream of the cage does not have enough momentum to keep the velocity gradient. Besides, the velocity profiles also vary with depth. At a deeper position, the velocity profile has smaller variations. However, the engineering approach proposed by Løland (1991) can only give an averaged estimation, but it cannot give the variations with depths and horizontal position.

Fig. 26 shows the flow velocity profiles on the X-Z plane with Y = 0 m at different X positions. The height of the velocity reduction region is 1.4–2 times of the fish cage height, and this height increases along the flow direction (X direction). Significant flow reductions are observed between the free surface and the bottom of the fish cage. The lowest velocity occurs near the free surface right behind the whole fish cage, as shown in Fig. 26(c). Below the fish cage (around Z = −6.4 m), the flow velocity slowly increases and reaches to slightly higher values than the undistributed flow velocity for all the presented profiles. This faster flow velocity may help to sweep away the fish faeces and uneaten feeds, but this may differ due to the terrains at different sites.

3.4.4. Elapsed time for numerical simulations

All the simulations presented in this study are performed on a desktop computer with an eight-core CPU, Intel® Xeon® CPU E5-2620 v4 @ 2.10 GHz, and 32GB memory. From the perspective of general computational efficiency, the elapsed time for running the numerical simulations is shown in Table 4. It shows that the elapsed time increases with the increasing number of elements and cells. Regarding the simulations of the two flexible net panels, the elapsed time in the study by Bi et al. (2014a) was 18 h, which is sixteen times longer than the elapsed time in the present study.

4. Conclusion

In the present study, a new coupling algorithm for fluid-structure interaction analysis of fluid flow through and around flexible nets is developed. The new coupling algorithm can benefit from the combination of Finite Element Method (FEM) and Finite Volume Method (FVM), and it can predict the structural responses of flexible nets and the surrounding flow field with high accuracy. The new coupling algorithm properly removes the additional data-fitting process for porous coefficients and adopts the Screen model to calculate the hydrodynamic forces. The two improvements can simplify the numerical procedures and improve the accuracy of numerical simulations. Besides, the new coupling algorithm employs the time-stepping procedure for the data transfer between the fluid and structural solvers and fulfils the law of momentum conservation. These two features ensure that the present method can achieve reliable results in both steady and unsteady conditions.

By applying the present coupling algorithm, Code_Aster and OpenFOAM can work together to simulate structural responses of the thin, flexible and high permeable nets in large aquaculture structures. Extensive validation studies are performed, considering different solidities, inflow angles, incoming velocity and dimensions of nets. In general, velocities in the wake region, deformations of nets and drag forces of the fish cage agree well with the validation data. Thus, the extensive validations in the present study provide strong confidence for users to apply the new coupling algorithm in a variety of numerical simulations related to the nets in aquaculture structures. Furthermore, the following conclusions are drawn based on the validation studies:

(1) The hydrodynamic force coefficients are vital for numerical simulations. As discussed in Section 3.2, the numerical results can have a large deviation up to 22.67% when $\theta = 75°$ if the employed C_D is unreliable. According to Section 3.3, the matching hydrodynamic force coefficients are essential to reproduce the experiments with high accuracy.
(2) A turbulence model is suggested to employ in the fluid model, in order to remove the unphysical sharp velocity gradient in the wake region. Hereby, the environmental loads on the downstream structures have small fluctuations, and the numerical simulations can easily achieve stable results.

(3) Compared to the engineering approach proposed by Løland (1991), which only approximates the wake effect as a flow reduction, the present coupling model can well address the wake effect on both the magnitude and direction of the fluid flow. Thus, the present coupling model can significantly improve the accuracy of numerical predictions.

CRediT authorship contribution statement

Hui Cheng: Conceptualization, Methodology, Software, Validation, Formal analysis, Investigation, Data curation, Writing – original draft, Writing – review & editing, Visualization. **Muk Chen Ong:** Conceptualization, Investigation, Resources, Writing – review & editing, Supervision, Project administration, Funding acquisition. **Lin Li:** Conceptualization, Investigation, Writing – review & editing, Supervision. **Hao Chen:** Conceptualization, Methodology, Investigation, Writing – review & editing.

Declaration of competing interest

The authors declare that they have no known competing financial interests or personal relationships that could have appeared to influence the work reported in this paper.

Acknowledgements

The authors would like to thank Digvijay Patankar from the Indian Institute of Technology, Jean Pierre Aubry from La Machine and the anonymous in the Code_Aster forum for providing help in using Code_Aster.

Appendix. Derivation of the velocity correction

In the present study, the hydrodynamic forces on nets are calculated using the forces model that is derived from experiments. According to the formulae (Eq. (6) and (7)), the hydrodynamic forces are functions of the undistributed incoming flow velocity $\boldsymbol{U}_{-\infty}$. While, in the FSI analyses, the fluid solver extracts the flow velocity at the centre of porous zones ($\boldsymbol{U}_c$). Thus, a process of velocity correction is needed to convert $\boldsymbol{U}_c$ to $\boldsymbol{U}_{-\infty}$, so that, the existing hydrodynamic force models can be applied in the simulations.

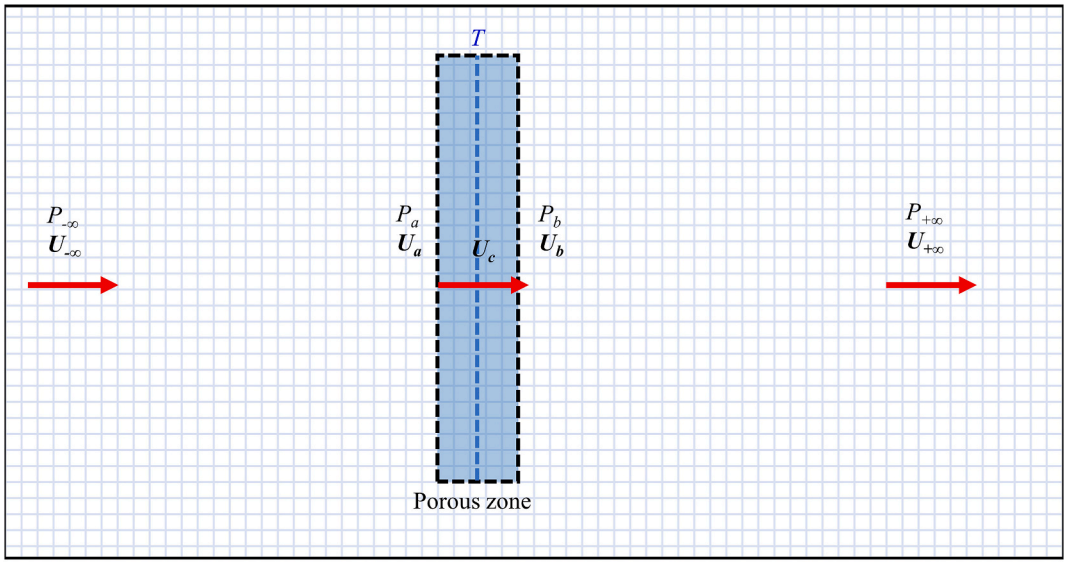

Fig. A1. Illustration of the notations for velocity and pressure. The black dash box represents a porous zone. The blue dash line is the centreline of the porous zone. T is the thickness of the porous zone.

The derivation is based on Bernoulli's principle without consideration of gravity. As illustrated in Figure A1, subscript a represents the variables (pressure and velocity) in front of the porous zone; subscript b represents the variables at the rear of the porous zone. The subscript ∞ represents the variables in the far-field, while -∞ represents the undistributed variables and +∞ represents the variables in the wake. Because the source term is only added to the cells in porous zones, it is reasonable to assume that the energy is constant along the streamlines that are in front of the porous zone and behind the porous zone. Thus, two Bernoulli equations can be achieved:

$$p_{-\infty} + \frac{1}{2}\rho_w(\boldsymbol{U}_{-\infty})^2 = p_a + \frac{1}{2}\rho_w(\boldsymbol{U}_a)^2 \tag{A1}$$

$$p_b + \frac{1}{2}\rho_w(\boldsymbol{U}_b)^2 = p_{+\infty} + \frac{1}{2}\rho_w(\boldsymbol{U}_{+\infty})^2 \tag{A2}$$

As shown in Figure A2, the pressure variations in front of and behind the porous zone are approximately equal. Thus, it is correct to assume that:

$$p_a - p_{-\infty} = p_{+\infty} - p_b \tag{A3}$$

The porous zone has at least one layer of cells, and the source term is added to the cell centroids. Approximately, the velocity is linearly reduced along the streamline in porous zones (from a to b) as the source terms are the same among the cells in a porous zone. The thickness of the porous zone is reasonably small compared to the length of the whole computational domain. Thus, it is proper to assume that:

$$\boldsymbol{U}_a + \boldsymbol{U}_b = 2\boldsymbol{U}_c \tag{A4}$$

The hydrodynamic force on the net panel causes a pressure jump across the porous zone. Based on Newton's Third Law, Eq. (A5) can be given. The

expression on the left-hand side of Eq. (A5) comes from the definition of drag force in laboratory experiments.

$$\frac{1}{2}C_D\rho_w A_t(\boldsymbol{U}_{-\infty})^2 = (p_a - p_b)A_t \tag{A5}$$

Eq. (A1) + Eq. (A2) can get:

$$p_b + p_{-\infty} + \frac{1}{2}\rho_w(\boldsymbol{U}_{-\infty})^2 + \frac{1}{2}\rho_w(\boldsymbol{U}_b)^2 = p_a + p_{+\infty} + \frac{1}{2}\rho_w(\boldsymbol{U}_{+\infty})^2 + \frac{1}{2}\rho_w(\boldsymbol{U}_a)^2 \tag{A6}$$

Combing Eq. (A6) with Eq. (A5), it can get:

$$p_{-\infty} - p_{+\infty} + \frac{1}{2}\rho_w(\boldsymbol{U}_{-\infty})^2 + \frac{1}{2}\rho_w(\boldsymbol{U}_b)^2 = \frac{1}{2}C_D\rho_w(\boldsymbol{U}_{-\infty})^2 + \frac{1}{2}\rho_w(\boldsymbol{U}_{+\infty})^2 + \frac{1}{2}\rho_w(\boldsymbol{U}_a)^2 \tag{A7}$$

If the pressures at the far-field ($p_{-\infty}$ and $p_{+\infty}$,) can be assumed approximately equal, then Eq. (A6) can be rewritten as:

$$(1 - C_D)(\boldsymbol{U}_{-\infty})^2 = (\boldsymbol{U}_{+\infty})^2 + (\boldsymbol{U}_a)^2 - (\boldsymbol{U}_b)^2 \tag{A8}$$

Eq. (A1) - Eq. (A2) can get:

$$p_{-\infty} - p_b + \frac{1}{2}\rho_w(\boldsymbol{U}_{-\infty})^2 - \frac{1}{2}\rho_w(\boldsymbol{U}_b)^2 = p_a - p_{+\infty} + \frac{1}{2}\rho_w(\boldsymbol{U}_a)^2 - \frac{1}{2}\rho_w(\boldsymbol{U}_{+\infty})^2 \tag{A9}$$

Combing Eq. (A9) with Eq. (A3), it can get:

$$(\boldsymbol{U}_{+\infty})^2 = (\boldsymbol{U}_b)^2 + (\boldsymbol{U}_a)^2 - (\boldsymbol{U}_{-\infty})^2 \tag{A10}$$

Replacing $(\boldsymbol{U}_{+\infty})^2$ in Eq. (A8) with Eq. (A10), it can get:

$$(2 - C_D)(\boldsymbol{U}_{-\infty})^2 = 2(\boldsymbol{U}_a)^2 \tag{A11}$$

Combing Eq. (A11) with Eq. (A4), the undistributed incoming flow velocity can be expressed as:

$$(\boldsymbol{U}_{-\infty})^2 = \frac{2}{(2 - C_D)}\left(\boldsymbol{U}_c + \frac{\boldsymbol{U}_a - \boldsymbol{U}_b}{2}\right)^2 \tag{A12}$$

As shown in Figure A2, $\boldsymbol{U}_c \gg \frac{\boldsymbol{U}_a - \boldsymbol{U}_b}{2}$. Thus, Eq. (A12) can be approximated as:

$$\boldsymbol{U}_{-\infty} = \sqrt{\frac{2}{2 - C_D}}\boldsymbol{U}_c \tag{A13}$$

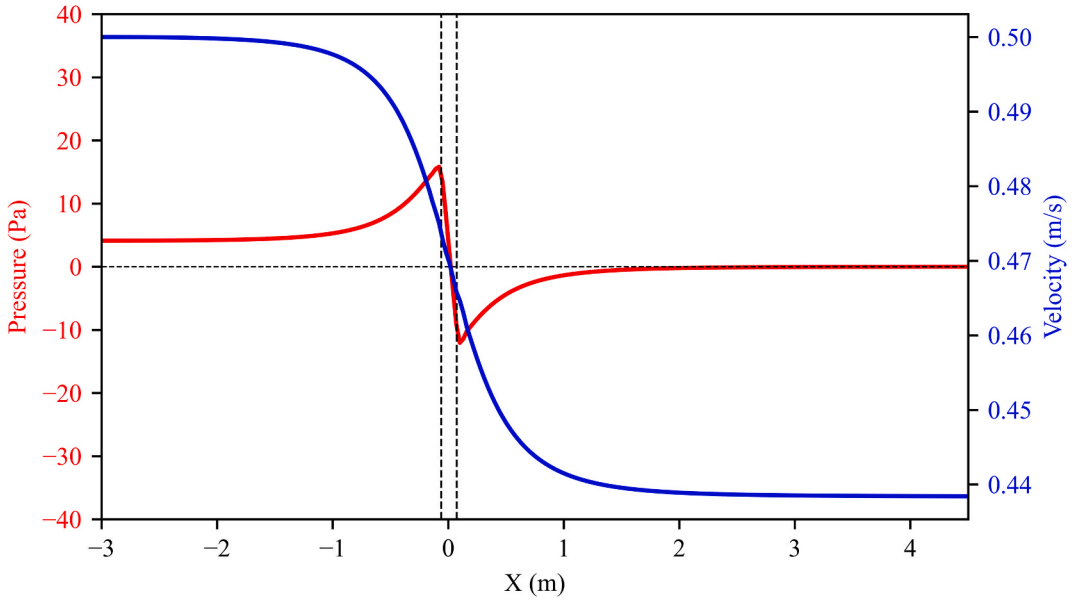

Fig. A2. Illustration of velocity and pressure distribution in front of and behind a net panel. The vertical dash lines represent the thickness of a porous zone.

One should notice that Eq. (A13) is derived based on the assumption that the flow direction is perpendicular to the net panel, *i.e.*, the inflow angle $\theta = 0°$. When $\theta \neq 0°$, the lift force should be considered. At this point, all the preceding derivation is still valid except that Eq. (A5) is changed to:

$$\frac{1}{2}(C_D + C_L)\rho_w A_t(\boldsymbol{U}_{-\infty})^2 = (p_a - p_b)A_t \tag{A14}$$

Therefore, the final relationship between $\boldsymbol{U_c}$ to $\boldsymbol{U_{-\infty}}$ is:

$$\boldsymbol{U}_{-\infty} = \sqrt{\frac{2}{2-(C_D+C_L)}}\boldsymbol{U_c} \tag{A15}$$

According to the experimental data by Bi et al. (2013) and Bi et al. (2014a), $\boldsymbol{U_c}$ can be acquired by averaging the velocities on the centrelines of the porous zones from Fig. 11 in Bi et al. (2013). C_D and C_L can be calculated by using Table 1 in Bi et al. (2014a). As shown in Table A1, the flow velocities calculated using Eq. (A15) agree well with the experimental results.

Table A1
Comparison of the flow velocity at the centre of a porous zone when $\boldsymbol{U_{-\infty}} = 0.17$ m/s.

Inflow angle	0°	30°	45°	60°
C_D	0.744	0.587	0.440	0.322
C_L	0.011	0.222	0.247	0.245
U_c*	–	0.135	0.134	0.139
U_c #	0.134	0.131	0.138	0.144
Deviation	–	−3.1%	2.9%	3.5%

U_c*: The velocities are averaged based on the centrelines of the porous zones in Fig. 11 from Bi et al. (2013).
U_c #: The velocities are calculated by using Eq. (A15).

References

Aarsnes, J.V., Rudi, H., Løland, G., 1990. Current forces on cage, net deflection. Engineering for offshore fish farming. In: Proceedings of a Conference Organised by the Institution of Civil Engineers, Glasgow, UK, vols. 17–18, pp. 137–152. October 1990.

Alver, M.O., Skøien, K.R., Føre, M., Aas, T.S., Oehme, M., Alfredsen, J.A., 2016. Modelling of surface and 3D pellet distribution in Atlantic salmon (Salmo salar L.) cages. Aquacult. Eng. 72 (73), 20–29. https://doi.org/10.1016/j.aquaeng.2016.03.003.

Antonutti, R., Peyrard, C., Incecik, A., Ingram, D., Johanning, L., 2018. Dynamic mooring simulation with Code_Aster with application to a floating wind turbine. Ocean Eng. 151, 366–377. https://doi.org/10.1016/j.oceaneng.2017.11.018.

Balash, C., Colbourne, B., Bose, N., Raman-Nair, W., 2009. Aquaculture net drag force and added mass. Aquacult. Eng. 41, 14–21. https://doi.org/10.1016/j.aquaeng.2009.04.003.

Bi, C.-W., Xu, T.-J., 2018. Numerical study on the flow field around a fish farm in tidal current. Turk. J. Fish. Aquat. Sci. 18 https://doi.org/10.4194/1303-2712-v18_5_06.

Bi, C.-W., Zhao, Y.-P., Dong, G.-H., Wu, Z.-M., Zhang, Y., Xu, T.-J., 2018. Drag on and flow through the hydroid-fouled nets in currents. Ocean Eng. 161, 195–204. https://doi.org/10.1016/j.oceaneng.2018.05.005.

Bi, C.-W., Zhao, Y.-P., Dong, G.-H., Xu, T.-J., Gui, F.-K., 2014a. Numerical simulation of the interaction between flow and flexible nets. J. Fluid Struct. 45, 180–201. https://doi.org/10.1016/j.jfluidstructs.2013.11.015.

Bi, C.-W., Zhao, Y.-P., Dong, G.-H., Xu, T.-J., Gui, F.-K., 2013. Experimental investigation of the reduction in flow velocity downstream from a fishing net. Aquacult. Eng. 57, 71–81. https://doi.org/10.1016/j.aquaeng.2013.08.002.

Bi, C.-W., Zhao, Y.-P., Dong, G.-H., Zheng, Y.-N., Gui, F.-K., 2014b. A numerical analysis on the hydrodynamic characteristics of net cages using coupled fluid–structure interaction model. Aquacult. Eng. 59, 1–12. https://doi.org/10.1016/j.aquaeng.2014.01.002.

Chen, D., Wang, C.M., Zhang, H., 2021. Examination of net volume reduction of gravity-type open-net fish cages under sea currents. Aquacult. Eng. 92, 102128. https://doi.org/10.1016/j.aquaeng.2020.102128.

Chen, H., Christensen, E.D., 2017. Development of a numerical model for fluid-structure interaction analysis of flow through and around an aquaculture net cage. Ocean Eng. 142, 597–615. https://doi.org/10.1016/j.oceaneng.2017.07.033.

Chen, H., Christensen, E.D., 2016. Investigations on the porous resistance coefficients for fishing net structures. J. Fluid Struct. 65, 76–107. https://doi.org/10.1016/j.jfluidstructs.2016.05.005.

Cheng, H., 2017. Study on the Anti-current Characteristics of a New Type Gravity Fish Cage and Design Optimising (Master Thesis). Ocean University of China, Qingdao, China.

Cheng, H., Li, L., Aarsæther, K.G., Ong, M.C., 2020. Typical hydrodynamic models for aquaculture nets: a comparative study under pure current conditions. Aquacult. Eng. 90, 102070. https://doi.org/10.1016/j.aquaeng.2020.102070.

Chu, Y.I., Wang, C.M., Park, J.C., Lader, P.F., 2020. Review of cage and containment tank designs for offshore fish farming. Aquaculture 519, 734928. https://doi.org/10.1016/j.aquaculture.2020.734928.

de Tullio, M.D., Pascazio, G., 2016. A moving-least-squares immersed boundary method for simulating the fluid–structure interaction of elastic bodies with arbitrary thickness. J. Comput. Phys. 325, 201–225. https://doi.org/10.1016/j.jcp.2016.08.020.

DeCew, J., Tsukrov, I., Risso, A., Swift, M.R., Celikkol, B., 2010. Modeling of dynamic behavior of a single-point moored submersible fish cage under currents. Aquacult. Eng. 43 (2) https://doi.org/10.1016/j.aquaeng.2010.05.002.

Faltinsen, O.M., Shen, Y., 2018. Wave and current effects on floating fish farms. J. Mar. Sci. Appl. 17, 284–296. https://doi.org/10.1007/s11804-018-0033-5.

Févotte, F., Lathuilière, B., 2017. Studying the numerical quality of an industrial computing Code: a case study on Code_aster. In: Abate, A., Boldo, S. (Eds.), Numerical Software Verification, Lecture Notes in Computer Science. Springer International Publishing, Cham, pp. 61–80. https://doi.org/10.1007/978-3-319-63501-9_5.

Food and Agriculture Organization, 2020. The State of World Fisheries and Aquaculture 2020: Sustainability in Action, the State of World Fisheries and Aquaculture (SOFIA). FAO, Rome, Italy. https://doi.org/10.4060/ca9229en.

Fridman, A.L., 1973. Theory and Design of Commercial Fishing Gear. Israel Program for Scientific Translations.

Gansel, L.C., McClimans, T.A., Myrhaug, D., 2012. The effects of fish cages on ambient currents. J. Offshore Mech. Arctic Eng. 134 https://doi.org/10.1115/1.4003696.

Gansel, L.C., Oppedal, F., Birkevold, J., Tuene, S.A., 2018. Drag forces and deformation of aquaculture cages—full-scale towing tests in the field. Aquacult. Eng. 81, 46–56. https://doi.org/10.1016/j.aquaeng.2018.02.001.

Griffith, B.E., Patankar, N.A., 2020. Immersed methods for fluid–structure interaction. Annu. Rev. Fluid Mech. 52, 421–448. https://doi.org/10.1146/annurev-fluid-010719-060228.

Halwart, M., Soto, D., Arthur, J.R., 2007. Cage Aquaculture – Regional Reviews and Global Overview (FAO Fisheries Technical Paper. No. 498). Roma.

Huang, L., Li, Y., Ni, Y., Cheng, H., Wang, X., Wang, G., Zhao, F., 2019. Study on the influence of mesh grouping on numerical simulation results of fish cages. In: Presented at the ASME 2019 38th International Conference on Ocean, Offshore and Arctic Engineering. American Society of Mechanical Engineers Digital Collection. https://doi.org/10.1115/OMAE2019-95706.

Jensen, B., Jacobsen, N.G., Christensen, E.D., 2014. Investigations on the porous media equations and resistance coefficients for coastal structures. Coast Eng. 84, 56–72. https://doi.org/10.1016/j.coastaleng.2013.11.004.

Jiang, C., Yao, J.-Y., Zhang, Z.-Q., Gao, G.-J., Liu, G.R., 2018. A sharp-interface immersed smoothed finite element method for interactions between incompressible flows and large deformation solids. Comput. Methods Appl. Mech. Eng. 340, 24–53. https://doi.org/10.1016/j.cma.2018.04.032.

Jones, W.P., Launder, B.E., 1972. The prediction of laminarisation with a two-equation model of turbulence. Int. J. Heat Mass Tran. 15, 301–314. https://doi.org/10.1016/0017-9310(72)90076-2.

Kristiansen, T., Faltinsen, O.M., 2012. Modelling of current loads on aquaculture net cages. J. Fluid Struct. 34, 218–235. https://doi.org/10.1016/j.jfluidstructs.2012.04.001.

Laws, E.M., Livesey, J.L., 1978. Flow through screens. Annu. Rev. Fluid Mech. 10, 247–266. https://doi.org/10.1146/annurev.fl.10.010178.001335.

Lee, C.-W., Kim, Y.-B., Lee, G.-H., Choe, M.-Y., Lee, M.-K., Koo, K.-Y., 2008. Dynamic simulation of a fish cage system subjected to currents and waves. Ocean Eng. 35, 1521–1532. https://doi.org/10.1016/j.oceaneng.2008.06.009.

Lekang, O.-I., 2019. Aquaculture Engineering, third ed. Wiley-Blackwell, Hoboken.

Li, L., Jiang, Z., Høiland, A.V., Ong, M.C., 2018. J. Offshore Mech. Arctic Eng. 140 https://doi.org/10.1016/j.oceaneng.2008.06.009.

Løland, G., 1991. Current Forces on and Flow through Fish Farms (Doctoral Thesis). The Norwegian Institute of Technology, Trondheim, Norway.

Martin, T., Kamath, A., Bihs, H., 2020. A Lagrangian approach for the coupled simulation of fixed net structures in a Eulerian fluid model. J. Fluid Struct. 94, 102962. https://doi.org/10.1016/j.jfluidstructs.2020.102962.

Moe-Føre, H., Christian Endresen, P., Gunnar Aarsæther, K., Jensen, J., Føre, M., Kristiansen, D., Fredheim, A., Lader, P., Reite, K.-J., 2015. Structural analysis of aquaculture nets: comparison and validation of different numerical modeling approaches. J. Offshore Mech. Arctic Eng. 137 https://doi.org/10.1115/1.4030255.

O'Neill, F.G., 2006. Source models of flow through and around screens and gauzes. Ocean Eng. 33, 1884–1895. https://doi.org/10.1016/j.oceaneng.2005.10.009.

Oppedal, F., Dempster, T., Stien, L.H., 2011. Environmental drivers of Atlantic salmon behaviour in sea-cages: a review. Aquaculture 311, 1–18. https://doi.org/10.1016/j.aquaculture.2010.11.020.

Patursson, Ø., 2008. Flow through and Around Fish Farming Nets (Doctoral Thesis) (Doctoral Thesis). University of New Hampshire, Durham, USA. https://scholars.unh.edu/dissertation/434.

Patursson, Ø., Swift, M.R., Tsukrov, I., Simonsen, K., Baldwin, K., Fredriksson, D.W., Celikkol, B., 2010. Development of a porous media model with application to flow through and around a net panel. Ocean Eng. 37, 314–324. https://doi.org/10.1016/j.oceaneng.2009.10.001.

Pepona, M., Favier, J., 2016. A coupled Immersed Boundary – lattice Boltzmann method for incompressible flows through moving porous media A coupled Immersed Boundary -Lattice Boltzmann method for incompressible flows through moving porous media. J. Comput. Phys. 321, 1170–1184. https://doi.org/10.1016/j.jcp.2016.06.026.

Peskin, C.S., 1972. Flow patterns around heart valves: a numerical method. J. Comput. Phys. 10, 252–271. https://doi.org/10.1016/0021-9991(72)90065-4.

Priour, D., 2014. Modelling axisymmetric codends made of hexagonal mesh types. Ocean Eng. 92, 1–11. https://doi.org/10.1016/j.oceaneng.2014.09.037.

Priour, D., 2013. A Finite Element Method for Netting: Application to Fish Cages and Fishing Gear, first ed. Springer Netherlands, Dordrecht. https://doi.org/10.1007/978-94-007-6844-4. 2013.

Reynolds, A.J., 1969. Flow deflection by gauze screens. J. Mech. Eng. Sci. 11, 290–294. https://doi.org/10.1243/JMES_JOUR_1969_011_036_02.

Rickard, G., 2020. Three-dimensional hydrodynamic modelling of tidal flows interacting with aquaculture fish cages. J. Fluid Struct. 93, 102871. https://doi.org/10.1016/j.jfluidstructs.2020.102871.

Robertson, E., Choudhury, V., Bhushan, S., Walters, D.K., 2015. Validation of OpenFOAM numerical methods and turbulence models for incompressible bluff body flows. Comput. Fluid 123, 122–145. https://doi.org/10.1016/j.compfluid.2015.09.010.

Roelofs, F., Shams, A., 2019. CFD—Introduction. In: Roelofs, Ferry (Ed.), Thermal Hydraulics Aspects of Liquid Metal Cooled Nuclear Reactors. Woodhead Publishing, pp. 213–218. https://doi.org/10.1016/B978-0-08-101980-1.00006-5.

SalMar ASA. (Accessed 11 October 2021).

Sim, J., Cheng, H., Aarsæther, K.G., Li, L., Ong, M.C., 2021. Numerical investigation on the cage-to-cage wake effect: a case study of a 4 × 2 cage array. J. Offshore Mech. Arctic Eng. 143, 051301 https://doi.org/10.1115/1.4049831.

Simonsen, K., Tsukrov, I., Baldwin, K., Swift, M.R., Patursson, O.E., Simonsen, K., Tsukrov, I., Baldwin, K., Swift, M.R., Patursson, O.E., 2006. Modeling flow through and around a net panel using computational fluid dynamics. In: OCEANS 2006. Presented at the OCEANS 2006, pp. 1–5. https://doi.org/10.1109/OCEANS.2006.306909.

Takagi, T., Shimizu, T., Suzuki, K., Hiraishi, T., Yamamoto, K., 2004. Validity and layout of "NaLA": a net configuration and loading analysis system. Fish. Res. 66 (2–3) https://doi.org/10.1016/S0165-7836(03)00204-2.

Tang, H., Hu, F., Xu, L., Dong, S., Zhou, C., Wang, X., 2019. Variations in hydrodynamic characteristics of netting panels with various twine materials, knot types, and weave patterns at small attack angles. Sci. Rep. 9, 1923. https://doi.org/10.1038/s41598-018-35907-1.

Tang, H., Xu, L., Hu, F., 2018. Hydrodynamic characteristics of knotted and knotless purse seine netting panels as determined in a flume tank. PLoS One 13, e0192206. https://doi.org/10.1371/journal.pone.0192206.

Tsukrov, I., Eroshkin, O., Fredriksson, D., Swift, M.R., Celikkol, B., 2003. Finite element modeling of net panels using a consistent net element. Ocean Eng. 30, 251–270. https://doi.org/10.1016/S0029-8018(02)00021-5.

Wang, S., Zhang, G., Zhang, Z., Hui, D., Zong, Z., 2017. An immersed smoothed point interpolation method (IS-PIM) for fluid-structure interaction problems. Int. J. Numer. Methods Fluid. 85, 213–234. https://doi.org/10.1002/fld.4379.

Wang, X., Zhang, L.T., 2009. Interpolation functions in the immersed boundary and finite element methods. Comput. Mech. 45, 321. https://doi.org/10.1007/s00466-009-0449-5.

Xu, Z., Qin, H., 2020. Fluid-structure interactions of cage based aquaculture: from structures to organisms. Ocean Eng. 217, 107961. https://doi.org/10.1016/j.oceaneng.2020.107961.

Yan, B., Wang, S., Zhang, G., Jiang, C., Xiao, Q., Sun, Z., 2020. A sharp-interface immersed smoothed point interpolation method with improved mass conservation for fluid-structure interaction problems. J. Hydrodyn. 32, 267–285. https://doi.org/10.1007/s42241-020-0025-1.

Yao, Y., Chen, Y., Zhou, H., Yang, H., 2016. Numerical modeling of current loads on a net cage considering fluid–structure interaction. J. Fluid Struct. 62, 350–366. https://doi.org/10.1016/j.jfluidstructs.2016.01.004.

Zhao, Y., Wang, X., Decew, J., Tsukrov, I., Bai, X., Bi, C., 2015. Comparative study of two approaches to model the offshore fish cages. China Ocean Eng. 29, 459–472. https://doi.org/10.1007/s13344-015-0032-0.

Zhao, Y.-P., Bi, C.-W., Dong, G.-H., Gui, F.-K., Cui, Y., Guan, C.-T., Xu, T.-J., 2013a. Numerical simulation of the flow around fishing plane nets using the porous media model. Ocean Eng. 62, 25–37. https://doi.org/10.1016/j.oceaneng.2013.01.009.

Zhao, Y.-P., Bi, C.-W., Dong, G.-H., Gui, F.-K., Cui, Y., Xu, T.-J., 2013b. Numerical simulation of the flow field inside and around gravity cages. Aquacult. Eng. 52, 1–13. https://doi.org/10.1016/j.aquaeng.2012.06.001.

Zhao, Y.-P., Li, Y.-C., Dong, G.-H., Gui, F.-K., Teng, B., 2007. Numerical simulation of the effects of structure size ratio and mesh type on three-dimensional deformation of the fishing-net gravity cage in current. Aquacult. Eng. 36, 285–301. https://doi.org/10.1016/j.aquaeng.2007.01.003.

Zhong, W., Li, X., Liu, F., Tao, G., Lu, B., Kagawa, T., 2014. Measurement and correlation of pressure drop characteristics for air flow through sintered metal porous media. Transport Porous Media 101, 53–67. https://doi.org/10.1007/s11242-013-0230-2.